Università degli Studi di Palermo

AREA RICERCA E INNOVAZIONE
SETTORE DOTTORATI E CONTRATTI PER LA RICERCA
U. O. DOTTORATI DI RICERCA

Ph.D. Mechanical, Manufacturing, Management and Aerospace Innovation (M3AI)
Dipartimento di Ingegneria (DI)
IMIS-01/A

A NUMERICAL AND EXPERIMENTAL FRAMEWORK FOR NON-INVASIVE AND CONTINUOUS MONITORING OF TRANSCATHETER HEART VALVES

IL DOTTORE
Silvia Puleo

IL COORDINATORE
Prof.ssa Giada La Scalia

IL TUTOR
Prof. Leonardo D'Acquisto

CO-TUTOR
Prof. Francesco Scardulla

CICLO XXXVIII
ANNO CONSEGUIMENTO TITOLO 2026

Abstract

Transcatheter aortic valve implantation (TAVI) has become the standard treatment for aortic stenosis, with increasing interest in its application to younger patients. Nonetheless, the long-term durability of transcatheter heart valves (THVs) remains a significant concern, as the progressive deterioration of the biological leaflets can impair their functionality. Conventional diagnostic imaging is insufficient for continuous functional monitoring, underscoring the necessity for non-invasive solutions for the early detection of valve dysfunction.

This thesis develops an integrated computational and experimental framework for designing and characterizing a non-invasive THV monitoring system utilizing photoplethysmographic (PPG) sensors and machine learning algorithms. A bidirectional fluid-structure interaction (FSI) analysis was conducted on an idealized aortic vessel model, both before and after the virtual deployment of a SAPIEN 3 Ultra valve, to evaluate the integration of optical fibers and PPG sensors. The simulations facilitated the identification of optimal sensor placement and demonstrated that pulse wave velocity and pulse transit time are effective metrics for assessing the transvalvular pressure gradient. Experimental assessment of the framework was performed using a 3D-printed aortic phantom and a pulsatile flow circuit, showing good agreement between numerical predictions and experimental data. Finally, a proof-of-concept system was developed in which a self-expanding Evolut FX valve was subjected to multiple hemodynamic scenarios generated through Latin Hypercube Sampling. PPG signals and flow variables were combined with machine learning models to predict the geometric orifice area of the valve and classify leaflet mobility, demonstrating high predictive capability and accurate discrimination between normal and pathological conditions.

Overall, this thesis establishes a unified methodological framework that integrates computational biomechanics, experimental investigation, and machine learning techniques for intelligent monitoring of valvular prostheses. This approach offers a promising tool for the early detection of valve dysfunction and the improvement of long-term management in patients undergoing TAVI, laying the groundwork for the development of smart prosthesis monitoring systems and the safe extension of the procedure to younger populations.

Acknowledgments

The study was funded by SiciliAn MicronanOTecH Research and Innovation CEnter SAMOTHRACE (MUR, PNRR-M4C2, ECS_00000022), spoke 3—Università degli Studi di Palermo S2-COMMs—Micro and Nanotechnologies for Smart & Sustainable Communities.

Contents

Nomenclature

Abbreviations

ALE – Arbitrary Lagrangian-Eulerian

AS – Aortic Stenosis

AVA – Aortic Valve Area

BHV – Bioprosthetic Heart Valve

CAD – Computer-Aided Design

CFD – Computational Fluid Dynamics

CT – Computed Tomography

EMAT – Electromechanical Activation Time

FEA – Finite Element Analysis

FEM – Finite Element Method

FSI – Fluid-Structure Interaction

GOA – Geometric Orifice Area

HALT – Hypoattenuated Leaflet Thickening

HLM – Healthy Leaflet Motion

IQR – Interquartile Range

IVI – IntraValvular Impedance

LBM – Lattice-Boltzmann Method

MAE – Mean Absolute Error

MCI – Model Confidence Index

MCL – Mock Circulatory Loop

MDCT – Multi-Detector Computed Tomography

NFC – Near Field Communication

PPG – Photoplethysmography / Photoplethysmogram

PTT – Pulse Transit Time

PVL – Paravalvular Leak

PWV – Pulse Wave Velocity

RFID – Radio Frequency Identification

RLM – Reduced Leaflet Motion

RMSE – Root Mean Squared Error

S3 – SAPIEN 3 Ultra

SAVR – Surgical Aortic Valve Replacement

STJ – Sinotubular Junction

SVD – Structural Valve Deterioration

SVM – Support Vector Machine

TAV – Transcatheter Aortic Valve

TAVI – Transcatheter Aortic Valve Implantation

TAVR – Transcatheter Aortic Valve Replacement

TEE – Transesophageal Echocardiography

THV – Transcatheter Heart Valve

List Of Figures

Figure 5.3 Two pulses from signal of proximal PPG 1 and distal PPG 2 from two cardiac cycle.

Figure 6.1 (A) Mock circulatory loop showing 1) the pulsatile pump, 2) adjustable valves, 3) pressure sensors, 4) THV device, 5) PPG sensors, 6) endoscopic camera, (7) compliance chamber, (8) electromagnetic flowmeter, (9) fluid collector; (B) photograph of the phantom model with device and attached PPG sensors.

Figure 6.2 Latin Hypercube Sampling of flow variables showing the variation of (A) systolic and diastolic pressure versus the heart rate, and (B) stroke volume versus the heart rate.

Figure 6.3 (A-C) Fluid pressure measurements at the inlet (grey line) and left subclavian artery (black line) for different flow scenarios and (D-F) corresponding PPG signals for three hemodynamic scenarios representing hypotensive (top), normal (middle), and hypertensive (bottom) flow conditions; the red and blue curves show PPG signals of sensors in the ascending and descending aorta, respectively; dots show peaks computed by the detecting algorithm; Note: SV = stroke volume, HR = heart rate; P_{sys} = systolic pressure; P_{dias} = diastolic pressure.

Figure 6.4 Representative photograph of THV leaflet opening with the GOA (red line) for three hemodynamic scenarios representing (A) hypotensive, (B) normal, and (C) hypertensive flow conditions.

Figure 6.5 (A) Scatter plot comparing predicted GOA values from the linear regression model with actual experimental GOA values; (B) confusion matrix showing the classification performance of the threshold-based model in distinguishing HLM versus RLM.

Chapter 1

1. Introduction

Aortic stenosis (AS) is the most common valvular heart disease in Western populations, with a prevalence that increases with age, reaching approximately 10% in people over eighty [1]. The disease is characterized by the progressive calcification of the aortic valve leaflets, which leads to narrowing of the valve orifice and, if left untreated, to heart failure. For decades, surgical aortic valve replacement (SAVR) has been the gold standard treatment, albeit at the cost of significant surgical trauma. The introduction of transcatheter aortic valve implantation (TAVI) has profoundly changed the therapeutic landscape [2], and advances in procedural techniques have broadened its indications to intermediate- and low-risk populations [3].

Despite these advantages, the long-term durability of transcatheter heart valves (THV) remains a significant concern. The leaflets, made from bovine or porcine pericardium, are subject to progressive degeneration due to cyclic loading, with a useful lifespan of 10–15 years [4]. Various mechanisms of malfunction, including leaflet thrombosis, paravalvular leak, and structural deterioration, can compromise their function [5–7]. These limitations are incompatible with the life expectancy of younger populations, and follow-up based on hospital imaging provides mainly morphological information. Therefore, there remains an unmet clinical need for long-term, non-invasive, and continuous monitoring strategies.

Computational modeling and numerical simulations have become increasingly important in the testing of biomedical devices [8, 9]. In the context of TAVI, fluid-structure interaction (FSI) techniques make it possible to describe the structural and hemodynamic behavior of

THVs in patient-specific models, allowing for the estimation of clinically relevant parameters such as the transvalvular pressure gradient. At the same time, experimental in vitro approaches, based on vascular phantoms and mock circulatory loop (MCL), play a crucial role in validating numerical models and in characterizing the hemodynamic performance of the device under controlled and repeatable conditions. The integration of in silico modeling and in vitro experimentation thus represents a predictive framework useful for identifying hemodynamic markers sensitive to valvular degeneration and potentially translatable into measurable physiological signals.

Recent advances in sensor miniaturization and telemetry have accelerated the development of remote telemonitoring systems for the functional assessment of valve prostheses [10]. Among the available technologies, photoplethysmographic (PPG) sensors, which can measure volumetric changes in blood in the subcutaneous vessels, offer a promising solution due to their flexibility, low cost, and ease of integration into wearable systems [11]. Other strategies proposed in the literature, including magnetic flow sensors, wireless pressure sensors integrated into the stent, and transvalvular impedance measurements [12–14], are based on active implantable devices and require more complex engineering standards compared to wearable solutions.

In light of these considerations, the research presented in this thesis aims to develop an integrated computational and experimental framework for the non-invasive monitoring of THV performance using PPG sensors, with the ultimate goal of identifying hemodynamic markers related to valve leaflet degeneration. The underlying hypothesis of the study is that appropriately configured PPG sensors, integrated with computational modeling and machine learning, can contribute to the characterization of the hemodynamic alterations associated with prosthetic dysfunction, providing complementary support to conventional diagnostic methods.

Thesis Outline

Chapter 2 – Cardiac Anatomy and Clinical Overview will provide an overview of the aortic valve, aortic stenosis, TAVI procedures, mechanisms of THV degeneration, and the principles of pulse wave propagation and photoplethysmography.

Chapter 3 – State of the Art will review the main methodologies for sensor-based THV monitoring, covering both numerical and experimental approaches.

Chapter 4 – Fluid–Structure Interaction Framework for Embedded Sensing in Prosthetic Valves will describe the development of the fluid-structure interaction (FSI) computational platform to assess the feasibility of using optical fibers and PPG sensors for monitoring device performance, based on flow and strain predictions.

Chapter 5 – From Numerical Markers to Experimental Measurement: Testbench and Protocol Design will present the translation of computational predictions into PPG metrics, the creation of a 3D printed aortic phantom, and the experimental protocol within a mock loop system.

Chapter 6 – Non-Invasive Monitoring of the THV through Photoplethysmography and Machine Learning will illustrate the proof-of-concept for continuous THV monitoring and the implementation of machine learning models for leaflet motion classification.

Chapter 7 – Conclusions and Future Perspectives will summarize the key findings of the research and discuss possible directions for future development.

Chapter 2

2. Cardiac Anatomy and Clinical Overview

2.1 Anatomy and physiology of aortic valve

The human heart is a muscular organ that functions as a twofold pump, feeding the pulmonary and systemic circulatory systems in turn. Within this system, the four heart valves (tricuspid, pulmonary, mitral, and aortic) function as mechanical gates that open and close in time with the cardiac cycle, maintaining unidirectional blood flow and avoiding retrograde reflux.

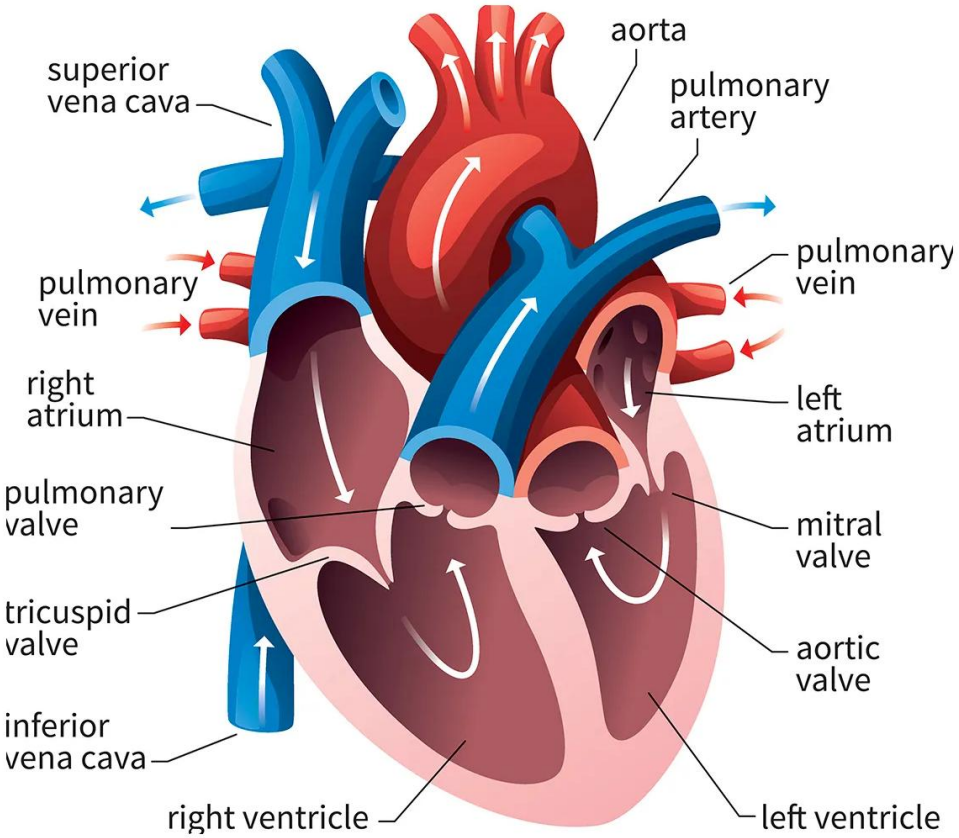

Figure 2.1 Anatomy of the human heart. Schematic representation of the cardiac chambers, major vessels, and valves, illustrating the direction of blood flow through the heart. Reproduced from Cardiology of Michigan [15].

The aortic valve, in particular, is a semilunar valve located at the interface between the left ventricle and the ascending aorta, responsible for regulating the passage of oxygenated blood to the entire body. It is a passive structure whose kinematic movement does not require external energy, being driven entirely by the pressure gradients generated during the contraction and relaxation phases of the myocardium. Anatomically, the valve is anchored within the aortic root, a complex structure that acts as a bridge between the left ventricular outflow tract and the ascending aorta. The fundamental anatomical components of the root include the aortic annulus (a virtual basal ring defined by the inferior attachment points of the leaflets), the sinuses of Valsalva, and the sinotubular junction (STJ), which marks the beginning of the tubular configuration of the aorta [16]. The sinuses of Valsalva are three expansions of the aortic wall located immediately above the annulus; two of them give rise to the coronary arteries.

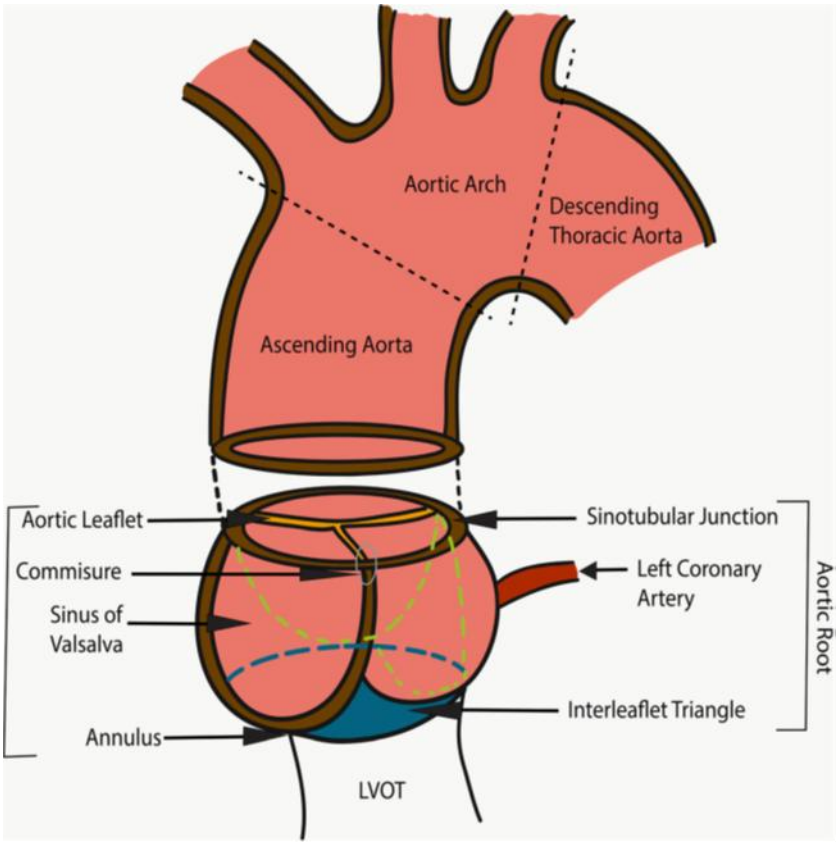

Figure 2.2 Anatomy of the aortic root and ascending aorta. The schematic highlights the aortic valve leaflets, sinuses of Valsalva, annulus, sinotubular junction, and coronary artery origins. Reproduced with permission from [17].

These structures are essential for valve dynamics as they facilitate the formation of vortices during systole, which prevent the leaflets from adhering to the aortic wall and support their rapid closure at the beginning of diastole. These vortices, originally hypothesised by Leonardo da Vinci, have been confirmed by modern in vivo magnetic resonance imaging techniques [18].

The valve is typically composed of three semilunar leaflets (right, left and non-coronary cusp) that have a sophisticated trilaminar configuration, which is essential for withstanding a hemodynamic load estimated at approximately 100,000 cycles per day [19]. The outermost layer, facing the aorta, is the fibrous layer, rich in organised collagen fibres that provide mechanical resistance to traction; the central layer is the spongy layer, composed of loose connective tissue and glycosaminoglycans that act as shock absorbers; finally, the layer facing the ventricle is the ventricularis, characterized by elastic fibres that allow flexibility and elastic return of the flaps.

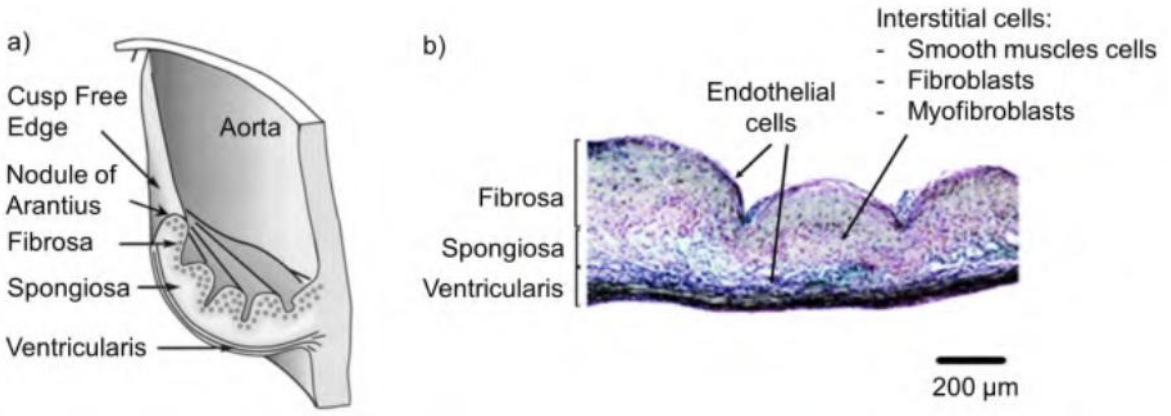

Figure 2.3 Histological organization of the aortic valve leaflet. The schematic and histological section illustrate the trilaminar structure of the valve leaflet (fibrosa, spongiosa, and ventricularis) and the distribution of endothelial and interstitial cells. Reproduced with permission from [20, 21].

During the systolic phase, ventricular pressure increases until it exceeds aortic pressure, pushing the leaflets outward and allowing blood to be ejected. Conversely, during the diastolic phase, the leaflets meet at the centre of the annulus to close the valve; a tight seal is ensured by the overlapping of the coaptation surfaces, called lunulae, and by the presence

of Arantius' nodule, a fibrous thickening located at the centre of the free edge of each cusp. Any structural or functional alteration in this complex apparatus can compromise hemodynamic balance, leading to severe clinical conditions such as stenosis or aortic insufficiency.

2.2 Aortic stenosis

Aortic stenosis (AS) is the most common valvular disease in Western populations and the third most common cardiovascular condition after hypertension and coronary artery disease [22]. This clinical condition is characterized by a pathophysiological narrowing of the aortic valve orifice, which obstructs the ejection of blood flow from the left ventricle to the ascending aorta during the systolic phase. In its early stages, AS can remain asymptomatic for years, earning it the label of ‘silent killer,’ as clinical symptoms — including dyspnoea, syncope, palpitations, and angina [23]— tend to manifest only when the reduction in valve area becomes significant, leading to a poor prognosis if not treated promptly. The aetiology of aortic stenosis recognises three main causes: calcific degeneration, congenital anomalies and rheumatic disease. Calcific degeneration is the most common form in elderly patients and results from degenerative remodelling of the valve leaflets due to fibrosis and progressive calcification, which typically begin between the sixth and eighth decades of life [24]. The pathogenesis of this form reflects the risk factors for atherosclerosis, involving chronic inflammation, lipid deposition and active calcification of the cusps, which compromise their mobility and increase their stiffness.

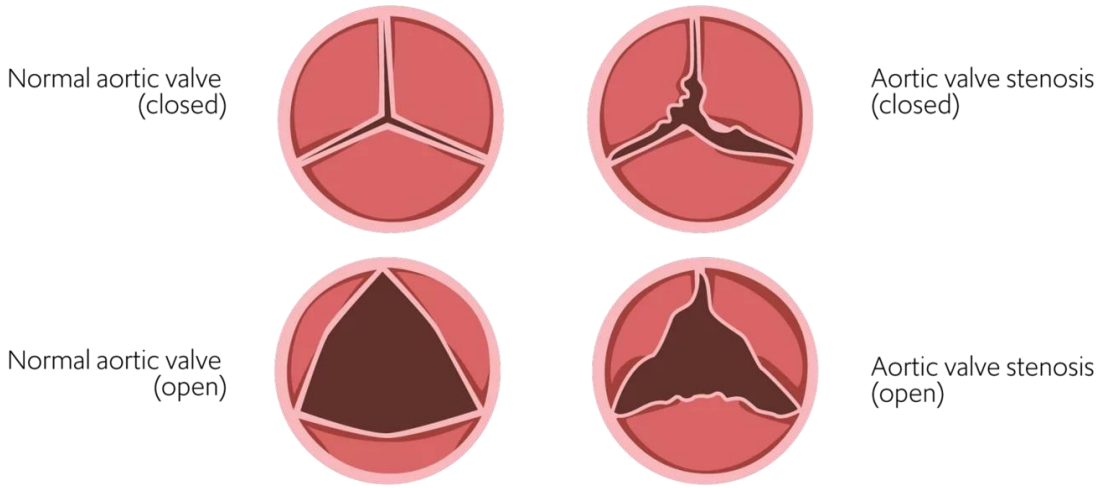

Figure 2.4 Normal and stenotic aortic valve. Schematic comparison showing leaflet thickening and reduced orifice area in aortic valve stenosis. Reproduced with permission from [25].

Congenital anomalies, such as a bicuspid aortic valve, predispose individuals to the early development of stenosis, often leading to clinical manifestation about twenty years earlier than in tricuspid valves due to localized mechanical stress and turbulent flow patterns [26]. Finally, rheumatic disease, although now rare in industrialized countries, remains a prevalent cause worldwide and is characterized by commissural fusion and thickening of the leaflets.

From a pathophysiological perspective, obstruction to ventricular outflow leads to increased resistance to flow, resulting in a higher transvalvular pressure gradient. To compensate for the increased afterload and maintain cardiac output, the left ventricle initially develops concentric hypertrophy. However, this reduces diastolic compliance and may progress to heart failure. The assessment of the severity of the condition is mainly carried out using Doppler echocardiography, which allows measurement of the peak velocity of the aortic jet, the mean pressure gradient, and the aortic valve area (AVA) [27].

According to current clinical guidelines, the severity of AS is classified into three main stages based on specific hemodynamic parameters [28, 29].

Table 1. Classification of AS severity. Adapted from [28, 29].

	Aortic Velocity (m/s)	Mean Gradient (mmHg)	Aortic Valve Area (cm^2)
Mild AS	2.0-3.0	<20	1.5-3.0
Moderate AS	3.0-4.0	20-40	1.0-1.5
Severe AS	>4.0	>40	<1.0

Mild stenosis is characterized by an aortic velocity between 2.0 and 3.0 m/s, a mean gradient less than 20 mmHg, and an AVA between 1.5 and 3.0 cm². Moderate stenosis features a velocity between 3.0 and 4.0 m/s, a mean gradient of 20–40 mmHg, and a valve area between 1.0 and 1.5 cm². Finally, severe aortic stenosis is defined by a peak velocity greater than 4.0 m/s, a mean pressure gradient greater than 40 mmHg, and a valve area less than 1.0 cm². In the presence of severe stenosis, valve replacement surgery — either surgical or transcatheter — becomes the only effective treatment option for restoring proper hemodynamic function and improving patient survival.

2.3 Transcatheter aortic valve implantation (TAVI)

For decades, surgical aortic valve replacement (SAVR) has represented the therapeutic gold standard for patients with severe aortic stenosis [29]. However, the highly invasive nature of this procedure—which requires median sternotomy, extracorporeal circulation, and pharmacological cardiac arrest—renders a significant proportion of patients, particularly the elderly or frail, ineligible for surgery due to the high operative risk. To address this clinical limitation, in 2002 Alain Cribier performed the first transcatheter aortic valve implantation (TAVI) in a human patient, ushering in a new era in the treatment of aortic valve disease [2].

TAVI represents a minimally invasive procedure that has revolutionized the management of aortic valve pathology, especially in patients at high surgical risk or deemed inoperable. During the procedure, a bioprosthetic valve is crimped and delivered via a catheter, typically inserted transfemorally, and deployed within the diseased native aortic valve without the need for open-heart surgery [2]. Unlike SAVR, the native calcified valve leaflets are not excised but are instead pushed aside by the expanding prosthesis, which anchors itself at the aortic annulus via radial force [30]. The procedure can be performed under local anaesthesia with conscious sedation, significantly reducing procedural risk and recovery time compared to traditional surgery [22].

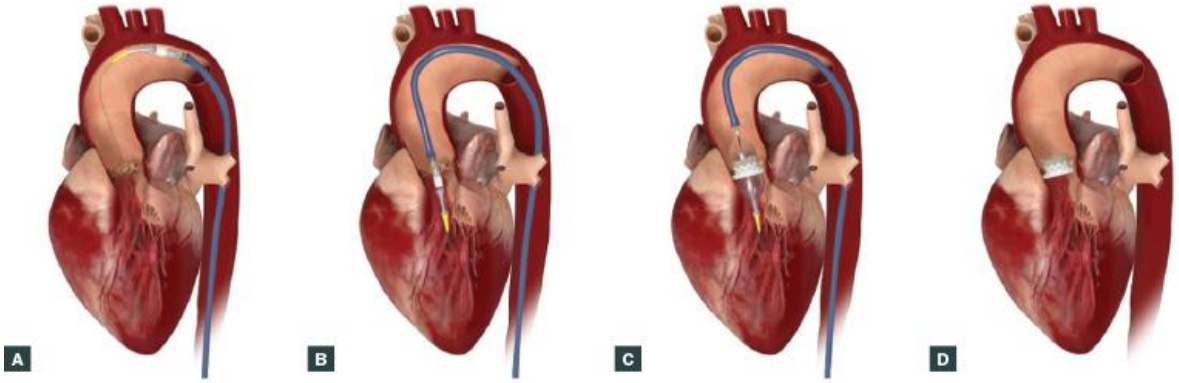

Figure 2.5 Key steps of the TAVI procedure via transfemoral access. (A) Catheter insertion and advancement through the aorta. (B) Positioning of the crimped bioprosthetic valve at the aortic annulus. (C) Valve deployment and expansion. (D) Final implant configuration after catheter removal. Adapted from [31].

Transcatheter heart valves (THV) share a common configuration designed to replicate the function of the native aortic valve while being deliverable through a catheter. They consist of three main components: a metallic stent, typically made of cobalt-chromium or nitinol, which anchors the device within the calcified native valve; bioprosthetic leaflets, usually made from bovine or porcine pericardium, mounted inside the frame to ensure unidirectional blood flow; and an external skirt, made of fabric or polymer, which minimizes paravalvular leak by filling the spaces between the stent and native anatomy [32].

THV can be classified by their expansion mechanism into two main categories: balloon-expandable and self-expandable valves. Balloon-expandable valves, the most prominent example being the Edwards SAPIEN family (Edwards Lifesciences, Irvine, CA), have a cobalt-chromium frame expanded by inflating a balloon, ensuring high radial force and precise positioning with immediate anchoring within the calcified annulus [33]. Self-expandable valves, such as the CoreValve/Evolut family (Medtronic, Minneapolis, MN), use a nitinol frame that gradually expands in response to temperature and mechanical release, providing continuous radial pressure that allows the device to adapt to changes in annular shape and size over time [34].

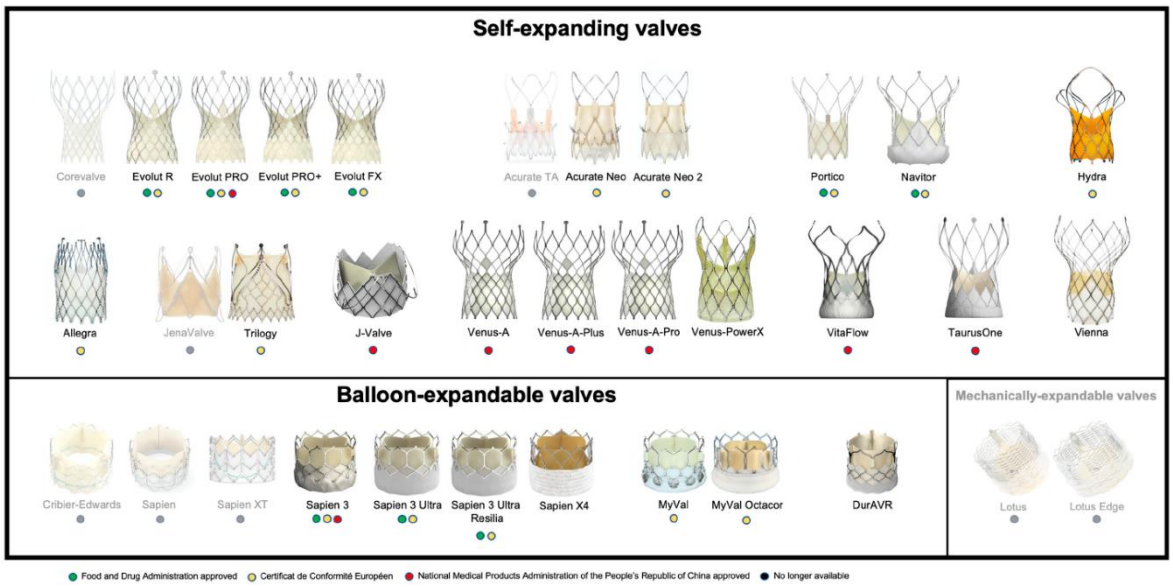

Figure 2.6 Commercially available transcatheter heart valves classified by expansion mechanism: self-expanding, balloon-expandable, and mechanically-expandable. With permission from Vinayak et al. [35].

From a hemodynamic perspective, self-expandable valves generally provide a larger orifice area and lower transvalvular gradients thanks to their supra-annular design, which allows for optimized blood flow; however, they are associated with a higher probability of permanent pacemaker implantation due to the pressure exerted on the cardiac conduction system [36]. Balloon-expandable valves, on the other hand, allow for more precise positioning and deployment, enabling a faster procedure, but tend to have a smaller effective orifice area, which can result in higher residual gradients [37]. These differences reflect the distinct

mechanical behaviors of each design and underscore the importance of customizing valve selection based on patient-specific anatomical and clinical characteristics [38].

Clinical evidence from randomized controlled trials has progressively expanded the indications for TAVI. Initially reserved for inoperable patients or those at high surgical risk, the procedure has shown comparable or superior results to SAVR in intermediate-risk patients in the PARTNER 2 [39] and SURTAVI [40] trials. Subsequently, the PARTNER 3 [41] and Evolut Low Risk [36] trials extended indications to low-risk patients, demonstrating comparable mortality and stroke rates between TAVI and SAVR at two years of follow-up. The NOTION trial, with a ten-year follow-up, confirmed the absence of significant differences in long-term clinical outcomes between the two treatments [42].

Despite remarkable advances, TAVI is not without complications, which remain a significant challenge. Paravalvular leak (PVL), which occurs in about 10% of patients, has been associated with increased mortality [43]. Conduction disturbances may require permanent pacemaker implantation in a variable percentage of patients (5% to 40%) depending on the type of device used [41]. Additional complications include coronary occlusion, vascular complications, and valve thrombosis [44]. However, with the progressive expansion of TAVI to younger and lower-risk populations, the central issue increasingly concerns the long-term durability of THV, which will be explored in subsequent paragraphs.

In summary, TAVI represents a transformative alternative that has significantly expanded therapeutic options for patients with severe aortic stenosis across all risk categories. Its ongoing evolution in device design, patient selection, and procedural techniques promises to further consolidate its role in the treatment of aortic stenosis. However, understanding the dynamics of THV degradation and implementing appropriate clinical follow-up strategies remain crucial to ensuring optimal long-term outcomes [45].

2.3.1 Dynamics of TAV degradation

The degradation of bioprosthetic heart valves, whether native or artificial, is a gradual process whose rate is neither constant nor uniform among different patients [46]. This variability makes the management of valvular diseases particularly complex and requires continuous monitoring of valve performance. THVs, sharing with surgical bioprosthetic heart valves (BHVs) the biological nature of the valve leaflets, are subject to similar mechanisms of structural deterioration, although with some peculiarities linked to the specific characteristics of the transcatheter procedure and device design.

Intrinsic failure modes related to the leaflet material are defined as Structural Valve Deterioration (SVD). Although the exact mechanisms of BHV and THV failure are not yet fully understood, calcification of the leaflets appears to be a major contributor to the degenerative process [47]. Leaflet calcification occurs mainly at the commissures and the lower portion of the cusps [48], and originates from a chemical interaction between the leaflet material and calcium ions present in the blood. Calcific deposits cause stiffening of the leaflet material, making them prone to mechanical damage such as tears and perforations [49].

Millions of cycles of repeated mechanical flexural stress within the leaflet material lead to wear and, at times, to tears in the leaflets themselves. Leaflet tears typically occur in regions of highest stress, usually at the interface between the leaflets and the stent posts of the support frame [50]. Fluid-structure interaction (FSI) simulation studies have shown that the highest stresses occur at the commissures and are significantly higher in the presence of stiff aortic walls, a condition common in elderly patients. Heart valves experience the highest hydrodynamic load during closure; therefore, a smooth and slow valve closure is crucial to keep these forces within acceptable limits and to prevent water hammer effects [51].

For THVs, additional specific mechanisms have been proposed that contribute to leaflet degradation and thrombosis [52]. Superficial damage to the leaflet material resulting from the crimping and expansion process during valve deployment causes microtears within the leaflet. The rougher surface, combined with collagen exposure, increases the thrombogenicity of the material. Non-physiological hemodynamics represents another contributing factor to leaflet thrombosis: excessive shear within the flow can activate platelets, which form clots when located in stagnant flow regions, typically at the base of the aortic sinus [53].

Failure modes not directly affecting the leaflet material are defined as non-structural valve deterioration and include valve thrombosis, endocarditis, and pannus formation. Valve thrombosis refers to the formation of clots on the surface of the valve, potentially impairing leaflet mobility and posing a risk of cerebrovascular obstructions from embolizing thrombi [54]. Endocarditis, an infection of the prosthetic valve, can lead to abscesses, fistulas, cusp rupture, and leaflet perforation, generally requiring valve replacement. Pannus formation consists of tissue growth leading to valve obstruction; although rare, it is a serious condition requiring surgical intervention and, unlike thrombosis, cannot be treated pharmacologically.

Studies on the long-term durability of BHVs have shown significant variability, with a marked decline in freedom from SVD after seven years following valve implantation [46]. Valve durability is severely limited in younger patients, in whom nearly half of valves required replacement within the first ten years after implantation. This inconsistent durability makes predicting the useful life of BHVs extremely difficult. Moreover, heart valve degradation typically presents an accelerating nature: once a critical threshold is crossed, a drastic deterioration is observed. Ross and Braunwald (1968) [55] published a landmark study on the dynamics of aortic stenosis, reporting that three-quarters of patients died within three years of symptom onset.

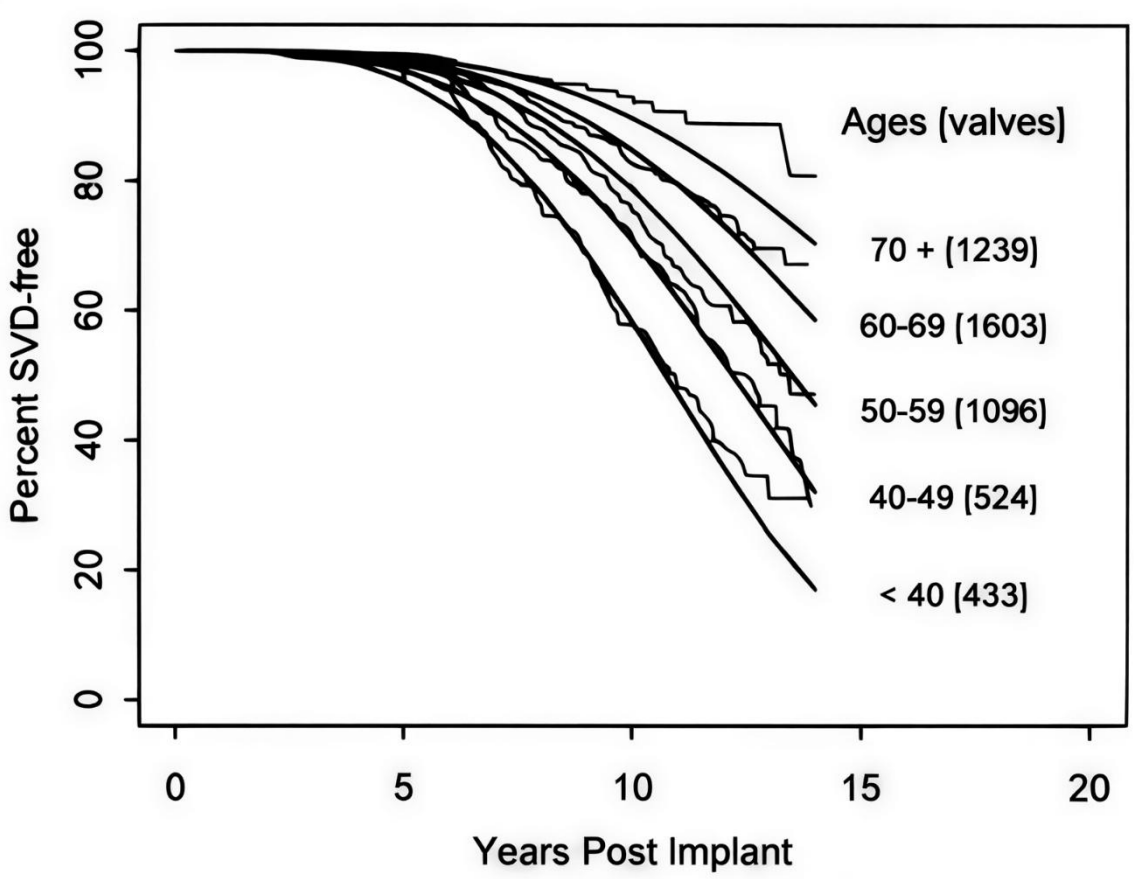

Figure 2.7 Freedom from SVD as a function of time and patient age at implantation for porcine bioprosthetic valves. Figure adapted from Grunkemeier et al.[46].

Regarding THVs in particular, although short- and medium-term results are encouraging, significant questions remain regarding long-term durability [45]. Registry data suggest that structural valve deterioration can occur within 5–10 years of implantation, especially in younger patients. The progressive expansion of TAVI to younger and lower-risk populations makes the emphasis on device durability increasingly imperative. Long-term data remain limited, as TAVI technology has been available for a shorter period than surgical valve replacement. Studies such as the PARTNER and Evolut low-risk trials are ongoing to provide more information about the long-term performance of THVs, with five- and ten-year data expected to confirm their durability [41].

The multitude of factors contributing to THV failure, including the common occurrence of SVD, and the complex interplay between fluid dynamics, biochemistry, and structural mechanics make managing THVs particularly challenging and require frequent assessment

of valve function. In cases of structural degeneration, the redo-TAVI procedure (implantation of a second THV within the first degenerated one) is often preferred over surgical explantation. However, this procedure presents particular risks: the second device displaces the degenerated leaflets of the first THV against the metal frame, creating a tubular structure that can extend into the sinuses of Valsalva or above the sinotubular junction, narrowing the anatomical space available for coronary flow [56]. These considerations underscore the importance of accurate and continuous clinical monitoring of patients with THVs.

2.3.2 Clinical Follow-Up for THV Monitoring

The clinical course of patients with THVs must be monitored periodically, with the interval between routine follow-up visits determined based on cardiac status, comorbidities, and other clinical factors. Diagnostic imaging represents the gold standard for assessing the structural integrity of THVs, although it is primarily limited to morphological analysis rather than a comprehensive functional evaluation. Several imaging techniques are available for detecting bioprosthetic valve dysfunction, including 2D/3D echocardiography and multi-detector computed tomography (MDCT) [57–59].

Echocardiography is the first-line imaging modality for detecting SVD and is the most accessible method for detecting serial changes in valve function. It is a ‘functional’ imaging modality, superior for demonstrating valvular hemodynamic, including increased transvalvular gradients and valvular regurgitation. According to the recommendations of the Valve Academic Research Consortium, echocardiography should be performed before discharge or within 30 days after valve implantation to establish baseline parameters, at 1 year post-implant, and annually thereafter [54]. Key Doppler echocardiographic parameters in assessing THV function in the aortic position include peak aortic jet velocity, mean and peak pressure gradients, doppler velocity index, effective orifice area, and the severity of valvular and paravalvular regurgitation [60].

Transthoracic echocardiography is the first-line test for post-procedural surveillance of THVs, allowing the evaluation of valve hemodynamic, the presence of aortic valvular and paravalvular regurgitation, biventricular function, and the function of other cardiac valves. Transoesophageal echocardiography (TEE) can enhance visualization of the prosthetic valve's morphological aspects and is particularly useful for assessing paravalvular regurgitation after TAVI [61]. However, TEE is an invasive method of evaluating device function, requiring sedation and presenting contraindications in certain patient categories.

MDCT provides anatomical and structural information that complements echocardiography and may be more sensitive in detecting early-stage valve thrombosis [62, 63]. Makkar et al. (2015) showed that subclinical leaflet thrombosis—detectable by computed tomography (CT) as hypoattenuated leaflet thickening (HALT)—is present in about 10-15% of patients after TAVI. HALT typically originates at the leaflet insertion points with variable extension toward the free edges and may result in reduced leaflet motion (RLM). CT is the gold standard for evaluating leaflet thickness and stent frame abnormalities, but it cannot determine aortic valvular gradients, thus its utility is limited for isolated SVD diagnosis. Cardiac CT is generally reserved for cases where valve dysfunction is suspected or when echocardiography yields inconclusive results.

Despite their established clinical utility, conventional imaging techniques have significant limitations that prevent their use for continuous THV monitoring. Early diagnosis and subsequent intervention may be challenging using standard imaging techniques such as TEE or 4D MDCT. These methods are cost-prohibitive, require specialized professionals, and are invasive (TEE) or involve exposure to ionizing radiation (MDCT), therefore precluding their routine use for continuous surveillance. Follow-up diagnostic imaging, although the standard for evaluating THV performance, is limited to morphological analysis rather than real-time functional assessment. Furthermore, imaging protocols require scheduled outpatient visits

and do not allow continuous monitoring of valve function between appointments. This gap is particularly relevant considering that valve degeneration is typically an accelerating process, with drastic deterioration observed once a critical threshold is crossed [55].

2.4 Pulse Wave Propagation in the Arterial System

Cardiovascular performance is the result of an intricate interaction between cardiac function and the elastic properties of the arterial tree. In the presence of aortic valve stenosis, the left ventricle is subjected to a double hemodynamic load: the valvular load, caused by the outflow obstruction, and the arterial load, related to the rigidity of the vascular system. Degenerative aortic stenosis frequently coexists with a noncompliant arterial system, as demonstrated by epidemiological studies and validated by the pathophysiological observation of numerous similarities with arteriosclerosis at the molecular level [64]. The implications of the elastic properties of the arterial tree and their dynamic variations in the natural history and prognosis of aortic stenosis, as well as in the success of its treatment, have generated great interest in the scientific community.

Arterial dysfunction is characterized by thickening of the wall, altered endothelial and autonomic function, and increased arterial stiffness. In particular, arterial stiffness represents a strong independent predictor of cardiovascular events and the development of target organ damage [65–67]. The gold standard for assessing arterial stiffness is aortic Pulse Wave Velocity (PWV), traditionally measured using invasive methods [68]. Brachial-ankle PWV is widely accepted as an indicator of arterial stiffness; an increase in PWV at rest is associated with the risk of cardiovascular events and mortality. A meta-analysis of 17 longitudinal studies demonstrated that a 1 m/s increase in aortic PWV corresponds to a 14-15% increase in the risk of total cardiovascular events, cardiovascular mortality, and all-cause mortality [65]. These results were confirmed by a subsequent meta-analysis with

individual data from 17,635 subjects [66]. Several studies have also reported significant associations between PWV values and prognosis in patients undergoing transcatheter aortic valve replacement [69–71]. It has been shown that PWV can be measured accurately during the TAVI procedure and used for post-procedural risk stratification [69], and that arterial stiffness can vary following the intervention [69, 70]. However, since it is not practical to measure PWV using invasive methods in most patients and given the relatively low reproducibility and high operator dependence of conventional non invasive techniques, current guidelines have concluded that routine measurement of PWV is not practical for widespread clinical use [72]. Therefore, there is a need to develop easy-to-use, low-cost methods for assessing arterial stiffness. To understand the physical principles underlying this assessment, it is necessary to examine the mechanics of the vascular wall and the laws governing the propagation of the pulse wave in the arterial system.

2.4.1 Arterial Mechanics and Vascular Distensibility

The aortic wall consists of three concentric layers (tunica intima, media, and externa); the tunica media, composed mainly of elastin, collagen, and smooth muscle cells, is the main determinant of the vessel's mechanical properties [73]. Elastin provides elasticity and resilience, collagen offers mechanical strength and limits distension at high pressures, while smooth muscle cells regulate vascular tone. Thanks to these elastic properties, the aorta plays a fundamental role in the transmission and modulation of the pressure wave generated by the left ventricle.

Contraction of the left ventricle generates a pulsatile pressure wave that propagates through the aorta and arterial system. The speed of propagation of this wave depends on the mechanical properties of the vascular wall, typically ranging between 4 and 15 m/s in the aorta. The fundamental relationship between pulse wave velocity and arterial distensibility is described by the Bramwell-Hill equation, formulated in 1922 [74]:

$$PWV = \sqrt{\frac{V \cdot dP}{\rho \cdot dV}} = \sqrt{\frac{1}{\rho \cdot DC}} \quad \text{Eq. 1}$$

where ρ is blood density, V is blood volume in the artery, P is blood pressure, and dV/dP represents arterial compliance. DC indicates the distensibility coefficient, defined as the fractional change in volume (or cross-sectional area) due to the change in pressure. The equation shows that PWV is inversely proportional to the square root of distensibility: stiffer arteries (lower compliance) have higher PWV values, since the pressure wave travels more quickly through vessels with less distensible walls.

The Bramwell-Hill equation can also be expressed in terms of change in pressure and vessel area:

$$PWV = \sqrt{\frac{\Delta P \cdot A}{\Delta A \cdot \rho}} \quad \text{Eq. 2}$$

where ΔP represents the change in pressure (or pressure gradient), A is the average area of the blood vessel, and ΔA is the change in vessel area during the cardiac cycle. This formulation is particularly useful in experimental applications where area changes can be estimated using imaging techniques such as ultrasound or magnetic resonance imaging.

Normal values of aortic PWV typically range between 5 and 10 m/s in healthy young adults, increasing with age and in pathological conditions such as hypertension [75]. Aging is associated with arterial stiffening due to changes in wall structure, leading to generalized stiffening of the arterial system. An increase in blood pressure is also associated with stiffer arteries [76].

2.4.2 Pulse Wave Velocity Measurement using Photoplethysmography (PPG)

Direct measurement of arterial stiffness typically requires determining compliance or distensibility from the pressure-volume or pressure-diameter curve, using ultrasound or

magnetic resonance imaging at a specific arterial site [67]. Arterial stiffness is thus usually assessed indirectly through Pulse Wave Velocity (PWV) or Pulse Transit Time (PTT).

Pulse Transit Time is defined as the time taken by the arterial pulse wave to propagate from one measurement site to another. Pulse Wave Velocity represents the speed of propagation of the wave and is calculated as the ratio between the distance traveled by the wave (d) and the PTT:

$$PWV = \frac{d}{PTT} \quad \text{Eq.3}$$

A reduced PTT (or increased PWV) is associated with stiffer arteries, according to the relationship established by the Bramwell-Hill equation. These metrics can be acquired using photoplethysmography (PPG), a non-invasive, low-cost, and easy-to-use optical technique that has the potential to meet the need for user-friendly methods for evaluating the mechanical properties of the arterial system, being suitable for routine clinical and home use, and potentially integrable into wearable devices [67].

Photoplethysmography measures variations in blood volume within a tissue vascular bed. Optical radiation is used to illuminate the peripheral tissue, where it is scattered and absorbed as it passes through the various tissue layers, before being transmitted or reflected from the surface. The attenuated light intensity is detected by an optical sensor and recorded as a voltage signal known as a photoplethysmogram (PPG). The raw PPG signal reflects variations in the attenuation of the incident optical radiation by different tissue components [67, 77].

The PPG waveform displays an almost-periodic pattern composed of one arterial pulse wave for each heartbeat, which resembles the arterial pressure wave, although there are important differences in the contour of the waveform. Each PPG pulse wave consists of two distinct

phases: the anacrotic phase and the catacrotic phase, corresponding respectively to the rising and falling edges of the signal [77].

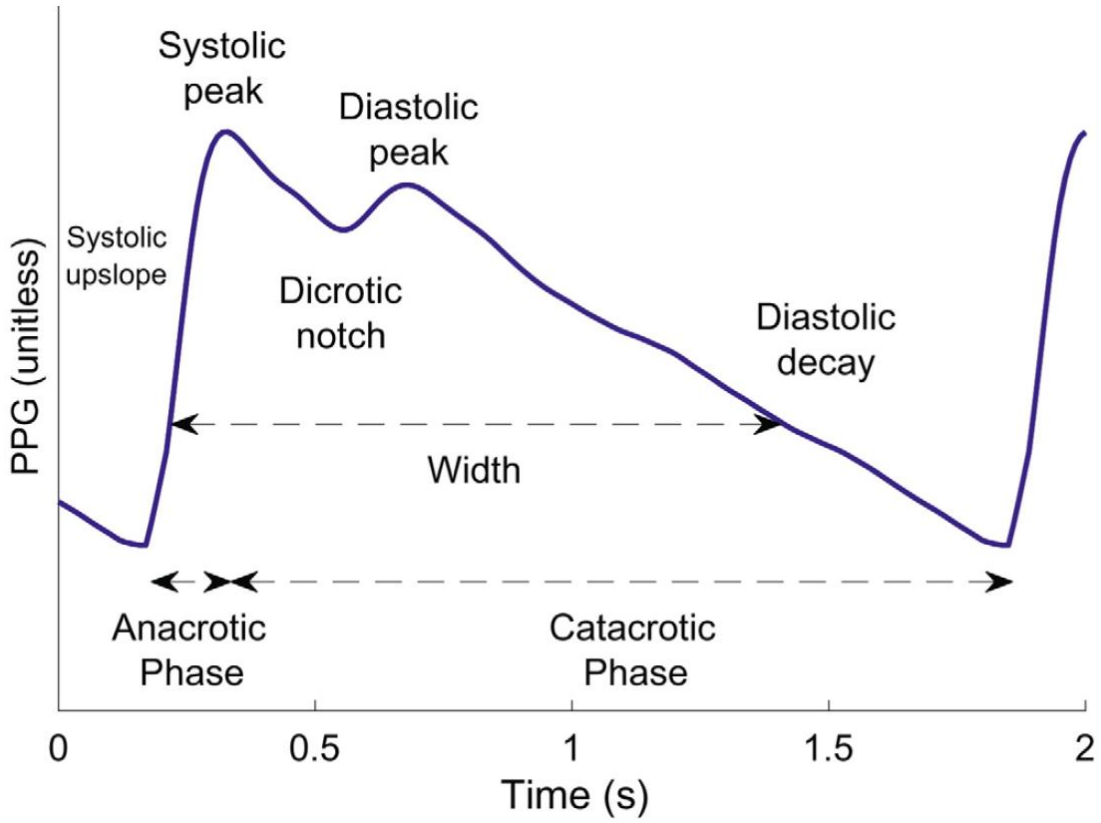

Figure 2.8 Schematic representation of a typical PPG pulse waveform, illustrating the key morphological features: systolic upslope, systolic peak, dicrotic notch, diastolic peak, and diastolic decay. The anacrotic and catacrotic phases correspond to the systolic and diastolic portions of the cardiac cycle, respectively. With permission from Kyriacou (2021) [78].

The anacrotic phase is dominated by systolic ejection: the rising systolic edge is caused by the expansion of the arterial system due to the influx of blood, and its slope is related to cardiac contractility. The systolic peak represents the point of maximum wave amplitude and corresponds to the moment when the blood volume detected by the sensor is highest. The catacrotic phase is characterized by the presence of the dicrotic notch, an inflection point on the falling edge marking the end of systole and the beginning of diastole. The dicrotic notch and the subsequent diastolic peak are caused by pulse wave reflections from the periphery, and their position and timing are influenced by arterial stiffness [79]. Diastolic decay is determined by the exponential contraction of the arterial system due to blood outflow and is influenced by vascular resistance and compliance. The morphology of the PPG pulse wave

is influenced by the characteristics of cardiac ejection (heart rate, rhythm, and stroke volume), cardiovascular properties (arterial stiffness and blood pressure), additional physiological processes such as respiration and the autonomic nervous system, and pathological conditions [77].

The PPG signal can be detected at multiple body sites, including the forehead, earlobes, forearm, wrist, fingertips, and toes [67]. PPG sensors can operate in transmission mode, where the tissue is positioned between the light-emitting diode and the photodetector (applicable to sites such as fingertips, earlobes, and toes), or in reflection mode, where the light emitter and photodetector are placed on the same side of the tissue, a configuration suitable for sites like the forehead, forearm, and wrist. However, the reflection mode is more susceptible to motion artifacts and is influenced by the position of the photodetector and the distance between the light emitter and photodetector [80–82]. PPG sensors can operate at different wavelengths, and the choice affects the depth of light penetration into the tissue. Infrared light (with a central wavelength around 940 nm) penetrates more deeply, while green light (about 520-530 nm) is more readily absorbed in the superficial layers, offering a better signal-to-noise ratio for skin-level measurements.

The PPG waveform provides the opportunity to assess arterial stiffness using both PTT measurement and waveform analysis (Pulse Wave Analysis), since the necessary instrumentation is low-cost and easy to use. Measuring PWV by means of PPG between two arterial sites requires simultaneous acquisition of PPG signals from two positions at a known distance along the arterial system. The PTT is determined as the time difference between corresponding characteristic points (typically the wave foot or systolic peaks) of the PPG waveforms captured by the two sensors. Knowing the distance between the measurement sites, the PWV can then be calculated according to the equation above.

Much of the research on photoplethysmography has relied on the analysis of signals acquired from clinical or in vivo trials, or from physiological signal databases. However, modifying clinical protocols or instrumentation can be costly in terms of time and resources. PPG simulators and phantoms offer the possibility to overcome these limitations, providing real-time signals with high repeatability and without the ethical considerations required for clinical and in vivo studies [83–85]. In a customized PPG phantom technology, numerous physiological parameters can be systematically controlled and varied, enabling complex study protocols and the analysis of the effectiveness of different signal processing techniques under various hemodynamic or vascular mechanical conditions. Such resources also enable investigation of the relationship between blood pressure, arterial stiffness, and PPG signal morphology in controlled conditions.

The characteristics of PPG technology—especially its non-invasive nature, low cost, and ease of implementation—make it a promising candidate for the development of long-term monitoring systems for transcatheter heart valves. The integration of PPG sensors into in vitro flow circuits with vascular phantoms could enable the characterization of the PPG signal's response to variations in hemodynamic parameters such as PTT and PWV, which may potentially indicate changes in valvular function. This approach fits within the broader context of the search for innovative solutions for the non-invasive monitoring of THVs, which will be discussed in the following chapter.

Chapter 3

3. State Of The Art

There is an unmet clinical need for the long-term monitoring of implanted THVs, in order to improve the management of patients undergoing TAVI and to safely extend this procedure to younger populations with a longer life expectancy. The development of methodologies for the non-invasive detection of malfunction in cardiac valve prostheses would represent an important support tool for clinical cardiologists, enabling timely interventions and improving patient outcomes. To address this need, numerical and experimental models have emerged as effective research tools for the design of prosthetic valves integrated with sensors [12, 13, 86–90], with growing interest in the development of battery-less sensors capable of real-time data transmission [91, 92].

3.1 Sensor-based THV monitoring solution

In recent years, several studies have proposed monitoring solutions for bioprosthetic valves based on different physical operating principles. An alternative approach to the use of diagnostic imaging for monitoring the functionality of valve prostheses after implantation can be represented by the use of sensor-based technologies integrated into the valve prosthesis itself or positioned nearby. Various attempts have been made to develop implantable or wearable devices for the continuous monitoring of THV functionality after implantation, with the aim of early detection of subclinical leaflet thrombosis and structural valve deterioration. Measurements of blood flow, acquired immediately downstream of the aortic valve, can provide relevant information for the early diagnosis of valve defects and bioprosthesis degeneration.

The investigation of sensor-based monitoring solutions has significantly evolved thanks to advances in both computational (in-silico) and experimental (in-vitro) methodologies. In-silico models are particularly promising in this context, as they offer the unique advantages of risk-free testing and virtual probing: expensive equipment such as high-speed cameras, optical systems, and test benches are not required; biological samples are not used for testing; and fluid dynamic parameters can be monitored simultaneously at hundreds of locations without any disturbance to the surrounding flow via virtual probes. At the same time, in-vitro experimental approaches allow for validation of signal acquisition and analysis methodologies under controlled and reproducible conditions, using phantoms and mock circulation loops that simulate physiological and pathological hemodynamic conditions. These complementary approaches enable researchers to simulate and test different sensor configurations, types of signals that can be acquired, and processing algorithms, generating evidence that integrates both clinical trials and conventional clinical practice.

3.1.1 Numerical approaches

Computational modelling has assumed an increasingly significant role in the study of transcatheter heart valves (THV) [93], offering the possibility to simulate in a controlled and reproducible manner the device deployment, post-implant blood flow, and interactions between the prosthesis and patient anatomy [94–98]. These in silico approaches generate complementary information with respect to in vitro experimentation and clinical trials, contributing to the understanding of the mechanisms governing valve performance and potential post-procedural complications. The three main categories of numerical simulation employed in this context are finite element analysis (FEA), computational fluid dynamics (CFD), and fluid-structure interaction (FSI) [99].

Finite element analysis (FEA) is used to model the mechanical behavior of devices and biological tissues under load. In the context of TAVI, FEA allows simulation of stent

expansion inside a calcified aortic root [100], prediction of stresses on the leaflets, and assessment of the risk of annular rupture or PVL [101]. Balloon-expandable and self-expanding valve frames can be virtually implanted into patient-specific anatomies to evaluate anchoring stability, radial forces, and potential device mismatch. Numerous studies have used FEA to investigate structural aspects of implantation, including crimping, recoil, and deployment, utilizing explicit and implicit solvers with different element formulations (hexahedral, tetrahedral, prismatic) [102, 103] and constitutive models for both the Nitinol frame (superelastic) and biological tissues (hyperelastic, elasto-plastic) [104, 105]. The typical workflow involves reconstruction of patient-specific anatomy from electrocardiogram-gated CT images, definition of constitutive models for the tissues and the device, and application of appropriate boundary conditions and constraints. FEA is particularly useful for device design optimization, reducing the risk of complications, and exploring clinical scenarios that are difficult to test in practice [104].

CFD focuses on the analysis of blood flow patterns through the valve and into the ascending aorta. By solving the Navier-Stokes equations in three dimensions, CFD models capture velocity fields, wall shear stresses, and turbulence generated by obstruction or non-optimal valve deployment [106]. In the context of TAVI, CFD makes it possible to quantify post-procedural hemodynamic, assess residual gradients, and estimate the risk of complications such as leaflet thrombosis or coronary obstruction [99]. The workflow typically involves using the deformed configuration resulting from the structural simulation of implantation as a geometric domain for flow analysis, with boundary conditions derived from clinical data or lumped parameter models [43, 107]. The setup of CFD models is simpler than FSI analyses; however, these simulations rely on rigid geometries, which may not adequately represent the complexities of device-host interaction within the fluid domain. Nevertheless, it has been shown that the aortic wall in TAVI patients exhibits significant stiffness, partially validating the assumption of rigid components in CFD simulations [108, 109].

Fluid-structure interaction (FSI) represents the integration of FEA and CFD, enabling simultaneous simulation of solid mechanics and fluid dynamics. In TAVI, FSI simulations can reproduce the interaction between moving leaflets and pulsatile blood flow, capturing realistic pressure-volume relationships and leaflet kinematics [110–112]. FSI is also applied for long-term durability assessment, estimating repetitive leaflet stresses and flow-induced fatigue. Although computationally more demanding, FSI provides the most comprehensive representation of the TAVI system and its physiological environment [43, 111, 113, 114].

Various approaches have been adopted to solve the coupled problem, including the Arbitrary Lagrangian-Eulerian (ALE) method [9, 101], the immersed boundary formulation [115], smoothed particle hydrodynamics [116], and the Lattice-Boltzmann Method (LBM) [8, 117], each with specific advantages regarding contact management, large deformations, and computational efficiency. The ALE method requires separate meshes for the fluid and solid subdomains, posing significant challenges in simulating the TAVI procedure where the valve's leaflets present transient contact. The immersed boundary formulation incorporates the solid subdomain entirely within the fluid domain, making it more suitable for large structural deformations and transient interactions between structures. Notably, the LBM represents a newer approach in the FSI field, in which the fluid is described by a set of particles distributed on a discrete lattice that move and interact according to simplified kinetic rules, encompassing a collision phase (where velocities adapt toward equilibrium via multi-relaxation time techniques) and a streaming phase (using bounce-back methods near walls) [118]. The LBM-FE coupling enables bidirectional FSI simulations where the fluid solver (e.g., XFlow, Dassault Systèmes) exchanges hydrodynamic forces and deformations with the structural solver (e.g., Abaqus), thus allowing for the simulation of valvular kinematics and hemodynamic performance post-TAVI in both idealized and patient-specific geometries. Morany et al. employed LBM coupled with FEM to simulate compliant aortic valves, demonstrating the versatility of this approach in cardiovascular biomechanics [117].

Verstraeten et al. developed and experimentally validated an FSI model for aortic stenosis using a finite-element-based CFD solver coupled with an implicit structural solver in LS-DYNA, showing the feasibility of FSI as a non-invasive tool to support clinical decision-making [119].

The use of numerical simulations is not limited to pre-procedural planning or device design optimization but also extends to the conceptual evaluation of innovative technologies for post-implant monitoring of THV. In this area, several studies have leveraged high-fidelity in silico modelling to explore the feasibility of sensor-integrated systems within prosthetic valves, combining fluid dynamic and structural simulations with machine learning techniques.

Bailoor et al. [13, 88] conducted a series of computational proof-of-concept studies aimed at evaluating the feasibility of a valve monitoring system based on pressure microsensors integrated onto the TAV stent. Using direct numerical simulations of transvalvular flow in idealized models of the ascending aorta—with two-way FSI coupling achieved via a sharp interface immersed boundary method—the authors simulated the response of healthy leaflets and those with reduced leaflet motion (RLM) under different flow conditions. In the first study [88], from a dataset of 21 simulations, it was shown that leaflets with RLM produce large, asymmetric pressure fluctuations in the region between the aortic sinus and the STJ. Using a linear classifier based on linear discriminant analysis and dimensionality reduction via principal component analysis, the authors achieved an accuracy greater than 90% in the prospective detection of individual leaflet dysfunction using only two discrete pressure measurements per leaflet. In the following study [13], the approach was extended to longitudinal monitoring, employing a logistic regression model on an array of 6 sensors integrated onto the stent, yielding high accuracy in both training and prospective validation. Overall, these works demonstrate that discrete blood pressure recordings on the TAV stent

can be effectively correlated with individual leaflet mobility using supervised machine learning techniques, laying the groundwork for an early detection system for valve deterioration.

Naccarata et al. [92] proposed a different approach for wireless monitoring of aortic valve prostheses, based on radio frequency identification (RFID) technology. From a numerical perspective, the authors leveraged electromagnetic simulations using the FEM to analyze the behavior of the metallic stent of the bioprosthesis as an antenna, evaluating the surface current patterns at 900 MHz and the electric field radiated on the thoracic surface. A numerical anthropomorphic model of the chest, including biological tissues with their respective electrical properties, was implemented in CST Microwave Studio to optimize the design of the trapezoidal coupling loop and maximize the trans-cardiac link's Transducer Power Gain. The simulations demonstrated the feasibility of a battery-free wireless RFID connection between the implanted valve and an interrogating antenna positioned on the skin, despite the implantation depth of around 7 cm in a highly lossy environment. This study stands out from the previous ones by employing electromagnetic rather than fluid dynamic simulations, addressing the monitoring problem from the perspective of wireless communication and energy harvesting.

Vennemann et al. [89] described how unsupervised novelty detection algorithms can be used to automate the interpretation of blood flow data for the early detection of valve deterioration. The proposed method was tested in an in vitro perfusion circuit that allowed simulation of a progressively degrading aortic valve by introducing increasingly severe aortic regurgitation using tubular inserts. Blood flow recordings, analyzed with a one-class Support Vector Machine (SVM) algorithm, enabled the definition of a diagnostic index (Model Confidence Index, MCI) capable of reflecting the severity of the deterioration: the median MCI dropped from 0.95 (baseline) to 0.72 for mild regurgitation, 0.40 for moderate,

and 0.17 for severe. Similar to Bailoor et al., this study also employs machine learning techniques for the automatic detection of valve deterioration; however, while Bailoor et al. relied entirely on computational FSI simulations, Vennemann et al. validated the methodology through direct measurements in an in vitro circuit. The unsupervised approach also offers the advantage of not requiring labeled datasets, generating self-calibrating and personalized models for each implant.

Overall, these studies highlight how numerical simulations—both in the form of high-fidelity FSI analyses and electromagnetic models—in combination with machine learning techniques, are opening new perspectives for continuous and non-invasive monitoring of cardiac valve prostheses.

3.1.2 Experimental approaches

Alongside the computational methods described in the previous section, numerous experimental studies have explored different physical sensing principles for the direct monitoring of heart valve prostheses functionality. These approaches range from vibro-acoustic and magnetic detection of leaflet dynamics to electromagnetic measurement of blood flow, intravalvular electrical impedance measurements, radiofrequency (RFID) backscattering, and multiparametric resistive sensing. Nearly all of these studies make use, as an experimental validation platform, of pulsatile-flow hydraulic circuits commonly referred to as mock circulatory loops (MCLs), which are briefly described below.

Mock circulatory loops are essential laboratory tools for the preclinical assessment of implantable cardiovascular devices, as they allow the in vitro replication of the physiological hemodynamic conditions of systemic circulation in a controlled and repeatable environment [120].

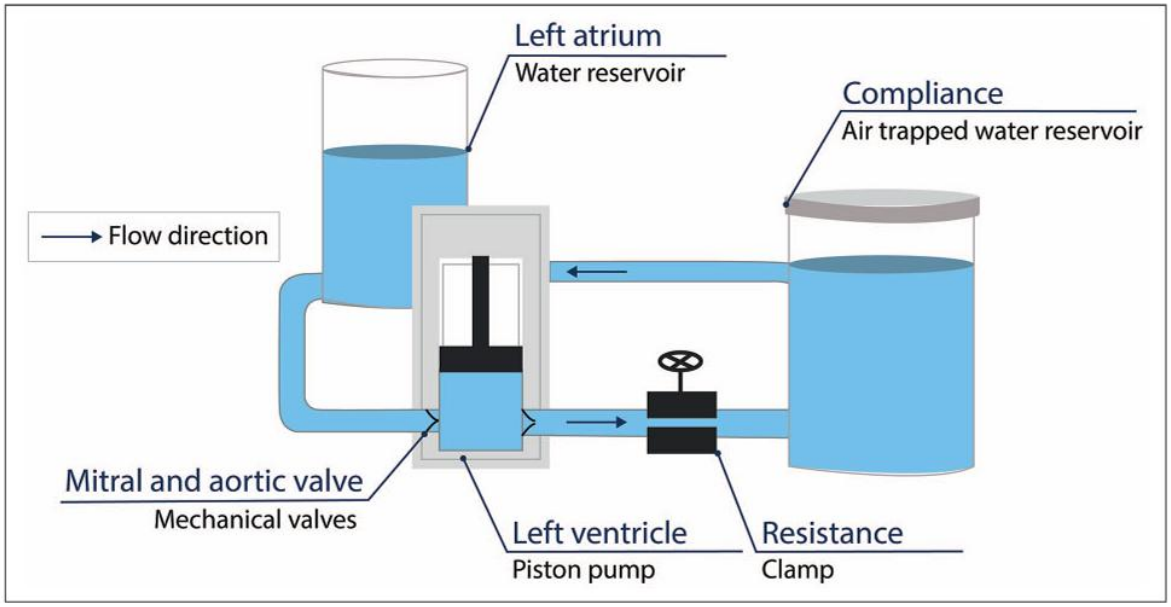

Figure 3.1 Mechanical mock circulatory loop simulating the systemic circulation, comprising a piston pump (left ventricle), mechanical valves (mitral and aortic), variable resistance, variable compliance, and a water reservoir (left atrium). With permission from Cappon et al. (2021) [121].

A MCL typically consists of a closed-circuit hydraulic system that replicates the main functional elements of the cardiovascular system: a pulsatile pump simulating the ejection function of the left ventricle, a compliance chamber that reproduces the elasticity of the arterial tree, a resistance element that emulates peripheral vascular resistance, and a reservoir serving as a venous pool. The physical foundation of these systems lies in the Windkessel model, which describes the behavior of the arterial tree as an elastic reservoir capable of storing blood during systole and gradually releasing it during diastole, thus ensuring the continuity of peripheral flow. The most common implementations use the three-element Windkessel model, which includes total arterial compliance, peripheral resistance, and characteristic impedance, thus allowing accurate simulation of pressure waveforms in the ventricle and aorta [122]. The compliance chamber can be constructed using various solutions, including air chambers, elastic silicone tubes, or piston-spring systems, each with specific advantages in terms of adjustability and faithful reproduction of physiological behavior.

Alongside purely mechanical circuits, ex vivo platforms have been developed that utilize explanted animal hearts, such as the cardiac BioSimulator, in which a porcine heart is connected to a pulsatile fluid dynamic system capable of reproducing realistic hemodynamic conditions in the presence of biological tissue. This provides an intermediate validation step between in vitro bench testing and in vivo experimentation. Overall, MCLs and ex vivo platforms have constituted the fundamental experimental infrastructure on which several valve sensorization studies have been conducted.

One of the first experimental investigations on the integration of sensors into valve prostheses was conducted by Lanning and Shandas [87], who proposed the concept of the smart heart valve. The sensitive element consisted of a thin-film piezoelectric transducer made of polyvinylidene fluoride, characterized by low mass, a wide frequency range and no need for external power. The sensors were mounted on the housings of mechanical and bioprosthetic valves and tested in a pulsatile-flow circuit. Joint time-frequency analysis of the vibro-acoustic signals demonstrated that the spectral content of closing sounds varied predictably in the presence of simulated thrombus or leaflet stiffening, providing the first experimental evidence for the feasibility of diagnostic monitoring based on sensors integrated into the prosthesis.

A different strategy was proposed by Rivero et al. [86], based on the integration of glass-coated amorphous Fe-based microwires directly into the cusps of the bioprosthetic valve. An external electromagnetic field at about 2 kHz excites the microwires, and the cyclic movement of the cusps modulates the amplitude of the signal detected by receiving coils and processed via synchronous demodulation. The system was validated in vitro on a hydrodynamic setup with a mitral bioprosthesis, demonstrating the capability to detect progressive alterations in leaflet mobility without the need for implanted electronics or power supply.

An advance towards an implantable and wireless system was reported by Vennemann et al. [12], with a batteryless blood flow sensor based on electromagnetic flowmetry. The device comprises a perivascular cuff with permanent magnets arranged in a Halbach ring configuration, generating a magnetic field perpendicular to the flow without requiring electrical energy. The voltage induced across two electrodes, proportional to the flow velocity according to Faraday's law, is transmitted via near field communication (NFC) to a smartphone that simultaneously powers the implant at 13.56 MHz, with consumption below 2 mW. Validation on a mock circulatory loop with a BHV achieved a sampling frequency of 60.2 Hz, demonstrating the feasibility of continuous, batteryless monitoring of aortic flow.

The concept of intravalvular impedance (IntraValvular Impedance, IVI) was introduced by the research group at the University of Bologna for the continuous monitoring of BHVs. The principle is based on miniaturized electrodes integrated into the valve structure: the local electric field is cyclically altered by the movement of the leaflets, producing measurable variations in impedance. In the first study [14], three prototypes with different electrode configurations were tested in vitro on a pulse duplicator, identifying the optimal configuration with electrodes placed at the valve commissures. Subsequently [123], the technology was validated ex vivo by implanting the sensorized BHV in an explanted porcine heart connected to a cardiac BioSimulator, confirming that the IVI signal remains detectable and consistent with the phases of the cardiac cycle even through biological tissue, and that its first derivative (dIVI/dt) provides information on the opening and closing speed of the leaflets.

A radically different approach was proposed by Naccarata et al. [92], based on turning the metallic stent of the bioprosthesis into an antenna. The meandered geometry of the wireframe is used as a UHF band loop antenna (860–960 MHz), electromagnetically coupled to a tiny loop harvester without mechanical connections to the valve. An on-skin patch antenna

interrogates the implanted prosthesis via RFID backscattering, establishing a completely battery-free trans-cardiac wireless link at a depth of about 7 cm. Numerical simulations and mock-up tests confirmed the feasibility of the connection despite losses in biological tissue.

A multiparametric sensing platform was presented by Kwon et al. [91], featuring an implantable, battery-free, and wireless system for the simultaneous monitoring of pressure, flow, and temperature. The biosensing module employs silicon nanomembrane strain gauges on a polyimide substrate, with a deflectable membrane pressure sensor and a 3D curved ribbon bidirectional flow sensor. Energy is harvested via NFC at 13.56 MHz, and data are transmitted via bluetooth low energy. The system was validated both ex vivo and in vivo in porcine and ovine models, demonstrating the ability to measure transvalvular pressure gradients at varying degrees of stenosis severity.

Finally, a complementary wearable approach was proposed by Liu et al. [90], using an external acoustic cardiography device that combines phonocardiogram and electrocardiogram to measure the electromechanical activation time (EMAT). In a prospective clinical study, EMAT decreased significantly after TAVR, correlating with the regression of left ventricular mass during follow-up up to 12 months. Although this approach does not directly monitor the valve, it offers a complementary non-invasive metric to assess the functional cardiac response to TAVR.

In summary, the experimental landscape of THV monitoring based on sensors is characterized by a diverse array of physical principles and levels of technological maturity. From early vibro-acoustic approaches [87] and magnetic sensing [86], through electromagnetic flowmetry [12] and intravalvular impedance [14, 123], to the antenna-enabled valve [92] and the silicon nanomembrane multiparametric platform [91], a clear progression toward wireless, battery-free, and multifunctional architectures can be observed. Most of these systems have been validated on mock circulatory loops and ex vivo platforms

like those described at the beginning of this section, and none has yet reached clinical use. Overall, these contributions define a rapidly evolving research field at the intersection of biomedical engineering, sensor technology, and cardiovascular medicine, providing the scientific foundation upon which the present thesis builds its own experimental and numerical investigations.

Chapter 4

4. Fluid–Structure Interaction Framework for Embedded Sensing in Prosthetic Valves

This chapter presents the multiphysics computational framework developed to assess the feasibility of integrating fiber optic sensors and photoplethysmography (PPG) sensors for monitoring the performance of the THV. The central hypothesis is that a suitably configured system of fiber optics and PPG sensors can be employed to quantify the structural and hemodynamic behavior of the SAPIEN 3 Ultra (S3) valve, with the ultimate goal of detecting deterioration in the biological valve leaflets. The model geometry, structural simulation of the TAVI procedure, post-implantation bidirectional FSI analysis, and the structural and flow measurements obtained from the numerical framework will be described in detail. The results of this chapter lay the foundations for designing the experimental test bench and measurement protocol described in Chapter 5, as well as for developing the non-invasive monitoring approach based on PPG and machine learning presented in Chapter 6. The content of this chapter is based on the work published in Puleo et al. [118].

4.1 Model Geometry

The Rhinoceros computer-aided design (CAD) software (Rhinoceros v.7, McNeel and Associates, Seattle, WA, USA) was utilized to create a CAD model of an idealized native aortic vessel. This model includes a three-dimensional representation of the tricuspid heart valve, incorporating the cusps, root, and sinuses, in alignment with the morphological characteristics and dimensions of a normal heart. The idealized vessel features a valve annulus diameter of 20 mm and a sinus diameter of 25 mm. Similarly, the configuration of

the aortic valve leaflets reflects the morphological shape of a normal aortic root, as previously documented [124]. To ensure a uniform flow regime, the proximal side of the left ventricle outflow tract and the distal portion of the ascending aorta were extended by eight times the vessel diameter. Figure 4.1A illustrates the dimensions of the CAD model of the idealized vessel.

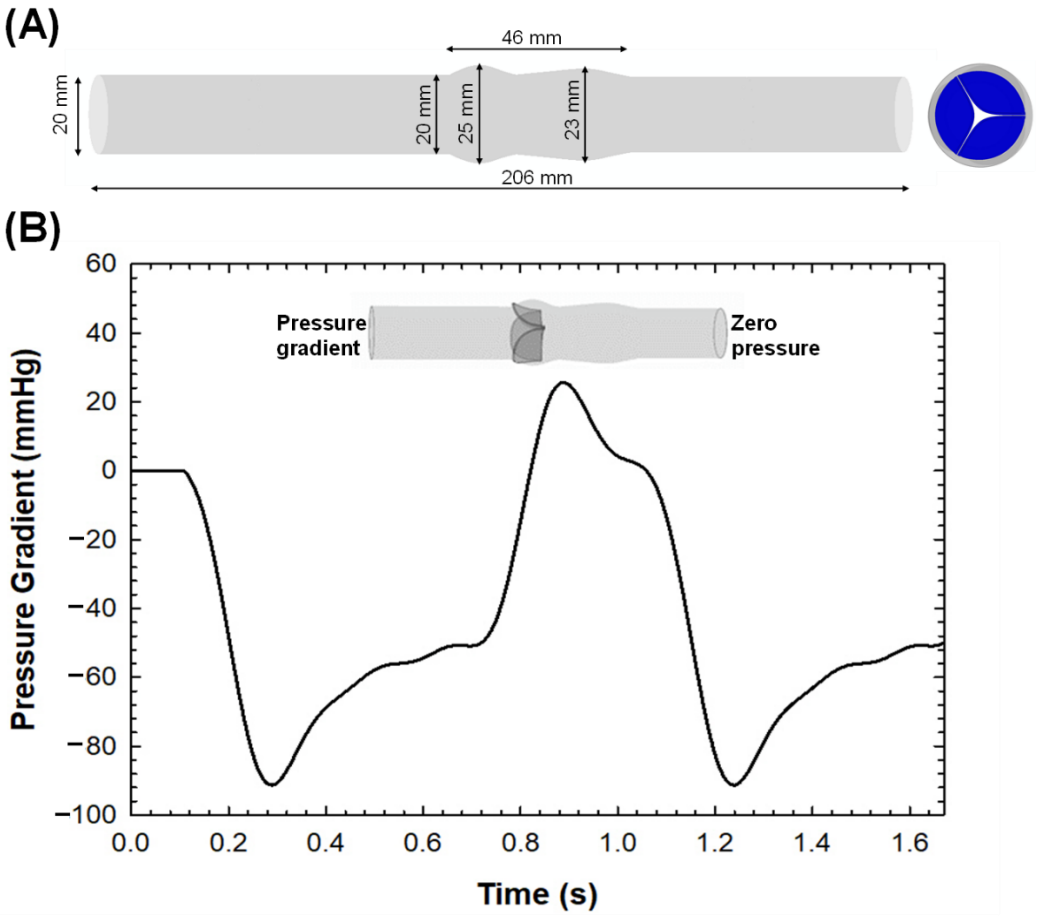

*Figure 4.1 (**A**) CAD model of the idealized aortic vessel with dimensions and cross-sectional view of the native valve geometry. (**B**) Time-dependent pressure gradient applied at the inlet surface as boundary condition for the FSI simulation.*

To simulate a transcatheter heart valve implantation (TAVI) procedure, the 23 mm SAPIEN 3 Ultra (S3) device (Edwards Lifescience, Irvine, CA, USA) was considered. The S3 device is a balloon-expandable device comprising a stent frame, a tri-leaflet valve, and a fabric skirt. The stent frame is constructed from cobalt–chromium material, the valve is made from processed bovine pericardial tissue, and the skirt is composed of polyethylene terephthalate material. The CAD model of the S3 device was generated by combining geometrical

measurements obtained from a high-resolution micro-computed tomography scanner with the reverse engineering of the metallic stent frame. The device valve leaflets were designed in accordance with CAD models described by Morganti et al. [95].

4.2 Simulation

The multiphysics simulation of TAVI was executed using a fully integrated two-way FSI analysis to assess metrics typically employed in evaluating the performance of bioprostheses. Initially, the deployment of the S3 device on an idealized vessel was determined through finite-element analysis using Abaqus/Explicit software (v2021hf7, Dassault Systèmes, Johnston, RI, USA). Subsequently, a two-way FSI analysis was developed to simulate the post-TAVI device performance by coupling Abaqus v2021hf7 (with a restart analysis) with an XFlow 2022 lattice Boltzmann fluid solver (Dassault Systemes, Simulia, USA). The lattice Boltzmann Method (LBM) is a computational technique used in fluid dynamics simulations, where the fluid is modeled as a collection of particles distributed on a discrete lattice grid. These particles move and interact based on simplified kinetic rules, which include: (a) collision, where particles' velocities are adjusted towards equilibrium using a multi-relaxation time technique [125], and (b) streaming, where particles move to adjacent grid points, employing the bounce-back method near walls [126].

4.2.1 Governing Equations and Coupling Strategy

The FSI framework adopted in this study couples a lattice Boltzmann fluid solver with a finite-element structural solver through a partitioned two-way co-simulation scheme.

The lattice Boltzmann method (LBM) describes the fluid motion through the evolution of particle distribution functions f_i on a discrete lattice, derived from the Boltzmann transport

equation [117]. In its discretized form, the distribution function at each lattice node is updated through a collision–streaming step:

$$f_i(\mathrm{r} + e_i\,\delta t, t + \delta t) = f_i(r, t) + \Omega_i \qquad \text{Eq. 4}$$

where f_i is the particle distribution function associated with the i-th discrete velocity direction, r is the position vector on the lattice, δt is the time step, e_i denotes the discrete velocity directions of the D3Q27 lattice model, and Ω_i is the collision operator, here implemented through the multi-relaxation time scheme proposed by D'Humières et al. [127]. The macroscopic flow variables are recovered from the statistical moments of the distribution function [101]:

$$\rho = \sum_i f_i \qquad \text{Eq. 5}$$

$$\rho u = \sum_i f_i\, e_i \qquad \text{Eq. 6}$$

where ρ is the fluid density, u is the macroscopic velocity, and e_i are the discrete velocity directions. The fluid pressure and the shear stress tensor follow as:

$$p = C_S^2 \rho \qquad \text{Eq. 7}$$

$$\sigma_{\alpha\beta} = -p\delta_{\alpha\beta} - \left(1 - \frac{1}{2\tau}\right)\sum_i (f_i - f_i^{eq}) e_{i\alpha} e_{i\beta} \qquad \text{Eq.8}$$

where C_S is the lattice speed of sound, τ is the relaxation parameter, $\delta_{\alpha\beta}$ is the Kronecker delta, and f_i^{eq} is the equilibrium distribution function obtained from a second-order expansion of the Maxwell–Boltzmann distribution under the low Mach number approximation. No-slip conditions at the solid walls are enforced through the bounce-back method [128].

On the structural side, the response of the solid components is governed by the equation of motion in its time-discretized explicit form:

$$M\ddot{u} + C\dot{u} + F_{int}(u) = F_{ext} \quad \text{Eq. 9}$$

where M is the mass matrix, C is the damping matrix, F_{int} is the internal force vector derived from the element stresses, F_{ext} is the vector of externally applied loads, and u is the nodal displacement vector.

The two domains are coupled through a partitioned approach with two-way coupling, employing the XFlow lattice Boltzmann solver for the fluid domain and Abaqus/Explicit for the structural domain, with data transfer between the two managed by the SIMULIA Co-Simulation Engine (Dassault Systèmes, Simulia Corp., Providence, RI). At each coupling increment, the flow solver computes the fluid traction, including pressure and viscous shear stress, on the wetted surfaces and transfers it as an external load to the structural solver. The latter then calculates the updated nodal displacements and returns the deformed geometry to the flow solver, which updates its boundary accordingly. This bidirectional exchange is repeated at every step until the end of the simulation, with the co-simulation interface surfaces defined as described in Section 4.2.3.

4.2.2 TAVI Structural Simulation

A quasi-static finite-element analysis was conducted by maintaining the kinetic to internal energy ratio below 10%. This was accomplished using a mass scaling technique with a stable time increment of 1.0 × 10−6 every 100 iterations. Additionally, a penalty contact algorithm with a friction coefficient of 0.1 was employed to facilitate contact during simulations among valve leaflets. The stent frame was meshed with structured hexahedral elements, as previously documented by our group [96, 129]. Stainless steel with bilinear elasto-plastic properties was used to model the metallic stent frame of the device. Linear elastic material

properties with a Young's modulus of 4 MPa were applied to the aortic wall and native valve leaflets. The aortic wall was modeled as a shell part with quadrilateral elements (S4R) and a material thickness of 2 mm. For the native valve leaflets, a 6-node linear triangular prism mesh (C3D6) was created by extruding shell elements with four layers through the thickness, assumed to be 0.5 mm thick. After simulating the deployment of the stent frame, the skirt was modeled by closing the stent frame cells with patch surfaces, which were connected to the device frame using tie contact conditions. Consequently, the valve leaflets of the S3 device were mapped onto the deformed stent frame. The Ogden constitutive law with a second-order polynomial form was used to model the biomechanical response of the pericardial tissue of the device valve leaflets, using μ_1= 0.00096 MPa, $\alpha_1 = -56$, μ_2 = 3.57 MPa, α_2 = 1.87, and $D_1 = D_2$ = 0.027 MPa [130].

The TAVI simulation involved simulating the device crimping, followed by the deployment of the S3 in the native valve leaflets, and concluded with a device recoil induced by the elastic material properties of the vessel. The crimping of S3 under frictionless contact conditions was performed using a cylindrical surface gradually moved radially from the initial device diameter of 23 mm to the final diameter of the closed device. After crimping, an elastic recoil of S3 Ultra was allowed to reduce internal energy before simulating valve deployment. For simplicity, the expansion of the S3 Ultra THV was achieved by radially displacing a cylindrical surface representing the expanding balloon's wall. Expansion was accomplished by enlarging the balloon surface to the device's nominal diameter of 23 mm. As boundary conditions, the proximal and distal ends of the aortic wall were fixed in all directions of the vessel. A viscous pressure of 1.0×10^{-6} MPa was applied to the inner surface of the device valve leaflets.

4.2.3 Post-TAVI Two-Way FSI Simulation

FSI analyses were conducted using the lattice Boltzmann finite-element method within a 3D model of an idealized vessel to examine the interaction between the fluid domain and solid components, such as the aortic wall and native valve leaflets. This FSI was specifically carried out to simulate both the kinematic behavior of the native valve and the performance of the device post-TAVI.

Following the deployment of the device, a restart analysis was executed in Abaqus to simulate a cardiac cycle lasting 0.8 seconds. This analysis enabled the incorporation of a structural simulation setting and the initial stress state at the conclusion of the device implantation. To facilitate data exchange between the structural and fluid solvers, a surface was defined to encompass the shapes of the device valve leaflets and the aortic wall, representing the FSI co-simulation interaction that allows for the exchange of fluid forces and deformations among different solvers.

A convergence analysis was performed to determine the optimal temporal and spatial discretization of the fluid domain, following the sensitivity approach described by Morany et al. [117]. Since both excessively coarse and excessively fine discretizations can introduce numerical instabilities in the coupled lattice Boltzmann–finite element scheme, the spatial-to-temporal resolution ratio dx/dt was adopted as the governing convergence parameter, while the flow velocity downstream of the valve was monitored as the reference output metric, together with the numerical stability of the two-way exchange. Several combinations of lattice size (resolved scale from 0.6 to 1.0 mm) and time step (from 1.0×10^{-5} to 5.0×10^{-5} s) were tested. Configurations with a high dx/dt ratio resulted in non-physical velocity values and early termination of the analysis, as the ratio of deformation speed to wave speed exceeded unity, whereas excessively low ratios produced numerical distortion at the fluid–structure interface. Convergence was achieved for a spatial-to-temporal resolution ratio of

dx/dt = 20, which ensured a stable two-way coupling and a physiologically consistent velocity field downstream of the aortic valve. Consequently, particles were distributed within the fluid domain with a spatial resolution of 0.001 m and a temporal resolution of 4.97×10^{-5} s. For the FSI simulation of native valve leaflets, the flow simulation was discretized using approximately 1 million D3Q27 lattices (27 × 28 × 209), with a high degree of freedom per discrete element and fourth-order spatial discretization. A slightly different discretization was applied for the post-TAVI FSI simulation, with a D3Q27 spatial discretization of 65 × 66 × 518. As boundary conditions, the pressure gradient between the left ventricle and the aorta (Figure 4.1B) was applied to the inlet surface, while a zero-pressure outflow condition was set for the outlet surface. A no-slip boundary condition was applied to the vessel wall. Two cardiac cycles were simulated for each FSI analysis.

4.3 Structural and Flow Measurement

An ideal polymeric optical fiber was incorporated around the vessel's circumference to detect structural deformation of the vessel. Due to their sensitivity to strain and temperature, optical fiber sensors are increasingly utilized in the biomedical sector [131], thanks to their compact size, lightweight nature, wearability, flexibility, and compatibility with biological tissues. The fiber was virtually placed downstream of the valve, following the vessel's circumferential direction, as this area exhibited the highest deformation in the FSI simulation of a healthy scenario. The fiber was modeled using truss elements (T3D2), assuming a linear elastic material behavior with a Young's modulus of E = 3000 MPa and a Poisson's ratio of $\nu = 0.49$ [132]. Tie contact constraints were employed to attach the fiber to the aortic vessel wall.

After completing the post-TAVI FSI simulation, the pressure data obtained were used to optimize the placement of the PPG sensors for device performance evaluation. Specifically,

two PPG sensors were positioned proximally and distally relative to the bioprosthesis. A script was developed in MATLAB (R2021a, The MathWorks Inc., Natick, MA, USA) to analyze the effect of the pressure gradient across the implanted device on pulse wave velocity (PWV) and pulse transit time (PTT). The model is based on the Bramwell–Hill equation, introduced in paragraph 2.4.1 (Eq. 2), in which ΔP represents the pressure gradient across the bioprosthesis, A the mean area of the vessel immediately downstream of the device, ΔA the difference between the maximum and minimum area of the vessel during the cardiac cycle, and ρ the density of blood. The PTT was calculated as the ratio between the distance between the PPG sensors and the PWV.

A parametric analysis was conducted to quantify the effect of varying pressure gradients on the PPG signal and the distances between PPG sensors. The script considers a range of distances between the PPG sensors, from 10 mm to 70 mm, to simulate different scenarios that can be replicated in experimental settings. The pressure gradients ranged from 4 to 15 mmHg, corresponding to the physiological range of pressure gradients across the S3 device. Understanding how PWV and PTT vary within this range can provide insights into the function of the aortic valve, particularly in distinguishing between normal function and functional stenosis.

4.4 Results

The sequence of steps involved in deploying the device is depicted for both axial and sagittal views of the idealized aortic vessel (Figure 4.2). Initially, the transcatheter heart valve (THV) is in a compressed state before being introduced into the aorta (Figure 4.2A). In the subsequent phase (Figure 4.2B), the valve begins to expand slightly as the crimping pressure is gradually released. Following this, the structural frame of the valve starts to take its designated shape (Figure 4.2C) until it fully engages with the aortic walls, ensuring proper

anchoring and alignment (Figure 4.2D). Consequently, the valve leaflets are mapped into the metallic stent frame to simulate the cardiac cycle.

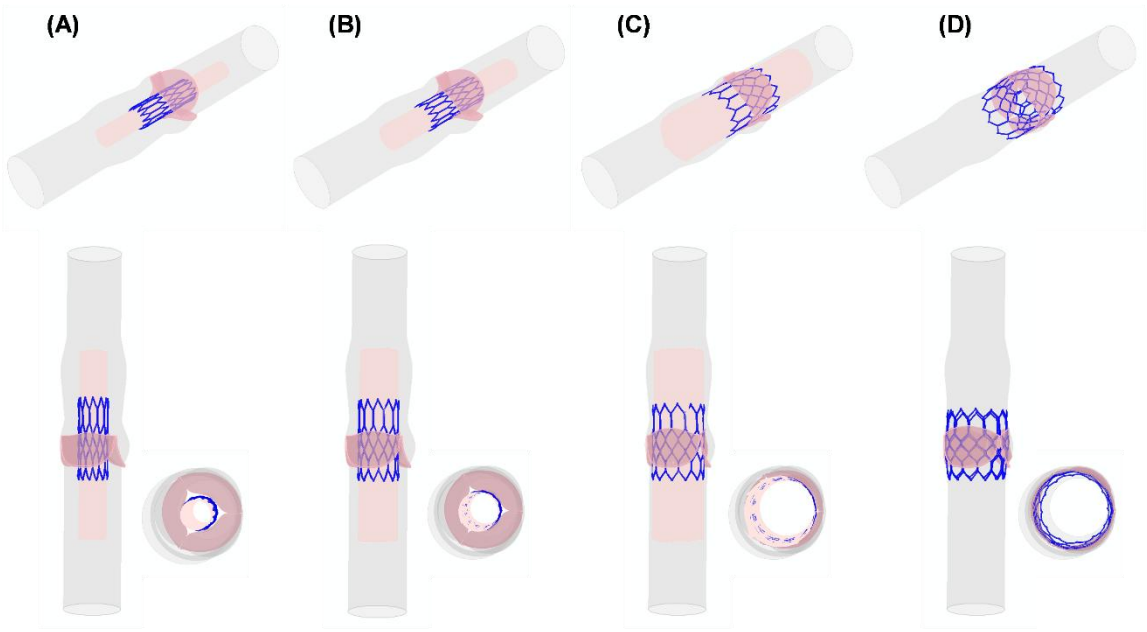

*Figure 4.2 Different steps of TAVI simulation; the deployment from the crimped THV to (**A–D**) expanded SAPIEN 3 Ultra: (**A**) Initial positioning of the crimped THV within the catheter. (**B**) Early stages of deployment as the catheter begins to release the THV. (**C**) Mid-deployment phase where the THV continues to expand further, making contact with the walls of the aorta. (**D**) Full deployment of the THV where the valve is completely expanded and positioned within the aorta.*

The flow velocity field, predicted using the multiphysics FSI simulation, is shown at different time points of the cardiac cycle for the ideal vessel with the native valve (Figure 4.3) and the bioprosthesis (Figure 4.4).

In the pre-TAVI simulation, at the onset of the systole phase (Figure 4.3A), the flow jet accelerates (Figure 4.3B) to reach its peak at systole. The flow field is characterized by a symmetric central jet with a maximum velocity of about 1.2 m/s (Figure 4.3C). During deceleration, a backward flow due to pressure drop leads to partial closure of the leaflets and flow acceleration, indicating a physiologically normal regurgitation (Figure 4.3D). As the fluid is forced to change direction or stop suddenly, a pressure drop occurs across the native aortic valve. In early diastole (Figure 4.3E), the velocity decreases, showing small flow magnitudes above the native aortic valve until the flow velocity nearly reaches zero (Figure 4.3F).

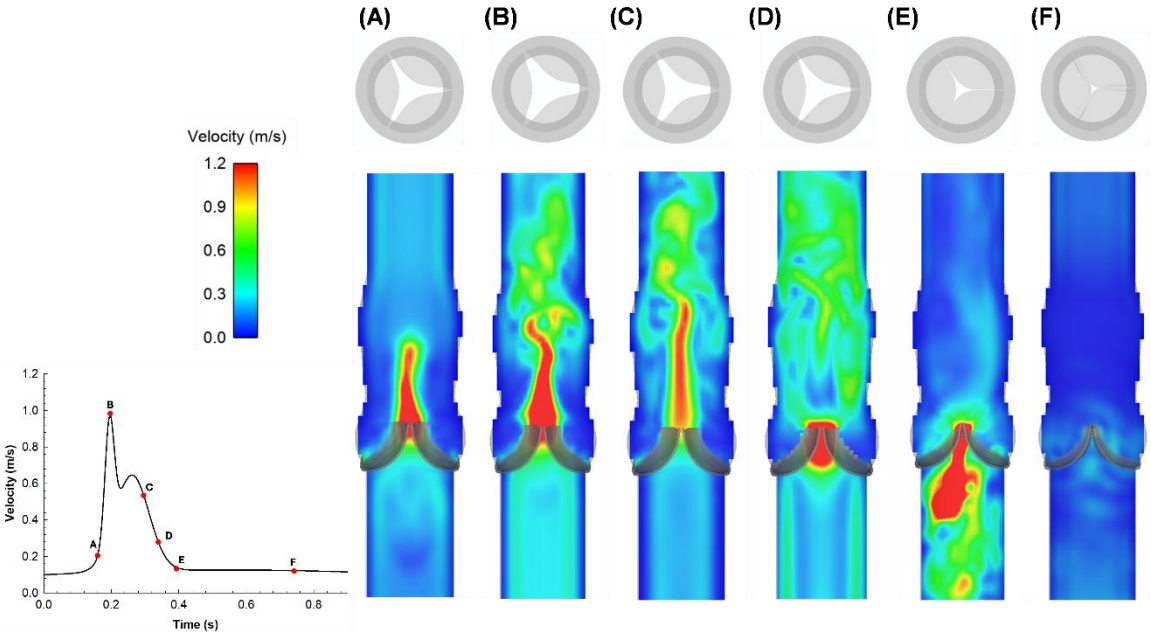

*Figure 4.3 FSI models using coupled LBM-FE: flow velocity at representative time points during native heart valve cardiac cycle (**A–F**). (**A**) Blood flow acceleration; (**B**) peak systole; (**C,D**) flow deceleration; (**E**) early diastole just prior the valve closure; (**F**) long diastole.*

In the post-TAVI simulation, the overall flow pattern resembles that of the native aortic valve, suggesting that the bioprosthesis helps restore physiological hemodynamics. Specifically, during the early systole phase (Figure 4.4A), the flow velocity field reveals high-velocity areas near the valve's central region, indicating the onset of turbulent flow patterns as blood begins to be ejected through the newly deployed THV. At mid-systole (Figure 4.4B), the velocity field starts to stabilize, with high-velocity areas more evenly distributed around the valve. Notably, the high flow values on the valve leaflet surfaces are likely due to numerical instabilities caused by the numerical method. In the late systole phase (Figure 4.4C), the flow velocity shows a more uniform distribution, indicating that the valve leaflets are fully open and the flow is becoming more streamlined. This trend continues until the end of the systole phase (Figure 4.4D), where further stabilization of the flow field is observed. During early diastole (Figure 4.4E), the valve leaflets begin to close, and the flow velocity field shows a significant reduction in velocity. In late diastole (Figure 4.4F), the low-velocity areas near the closed valve demonstrate the valve's ability to prevent backflow.

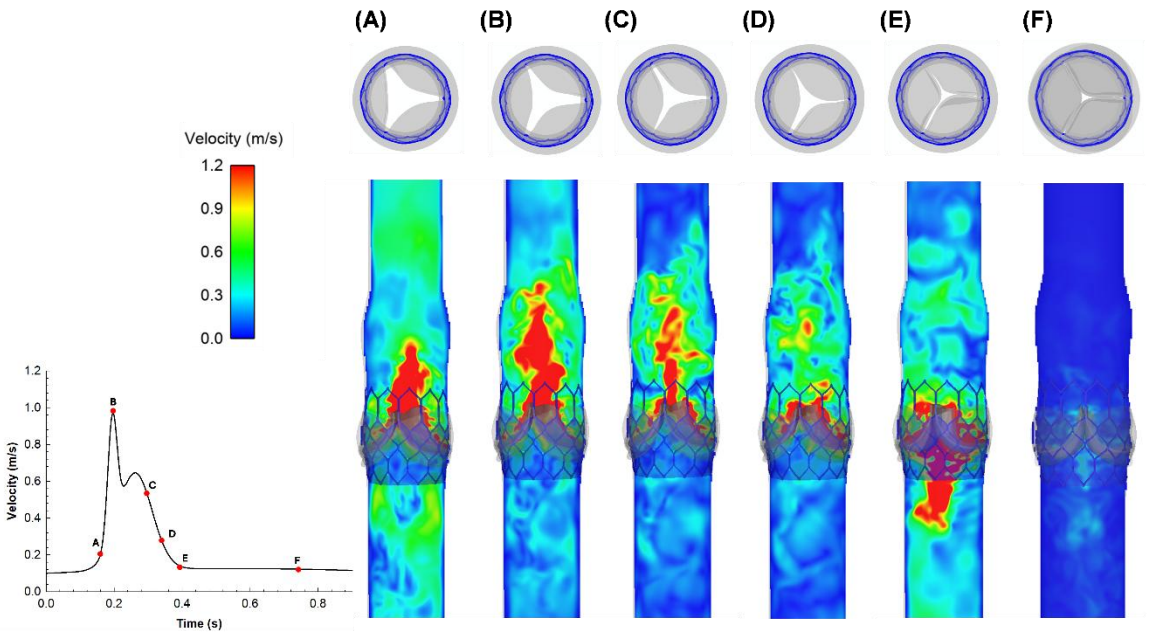

*Figure 4.4 FSI models using coupled LBM-FE: flow velocity field at representative time points (**A–F**), post-TAVI procedure. (**A**) Fluid acceleration, (**B**) systolic peak; (**C,D**) deceleration; (**E**) early diastole and (**F**) long diastole.*

Following the TAVI procedure, the engineering strain distribution in the circumferential direction was examined to identify the area of the vessel experiencing the highest deformation, thereby determining the best location for the optical fiber sensor (Figure 4.5A). The highest circumferential strain was found near the sinuses and sinotubular junction during peak systole, in the contact region of the aortic root with the optical fiber downstream of the valve, as well as in the contact area between the aortic root and the native valve leaflets. Figure 4.5B illustrates the circumferential strain profile along the optical fiber's length over time. At peak systole, a maximum circumferential strain of 3% was recorded when the optical fiber was positioned along the sinotubular junction.

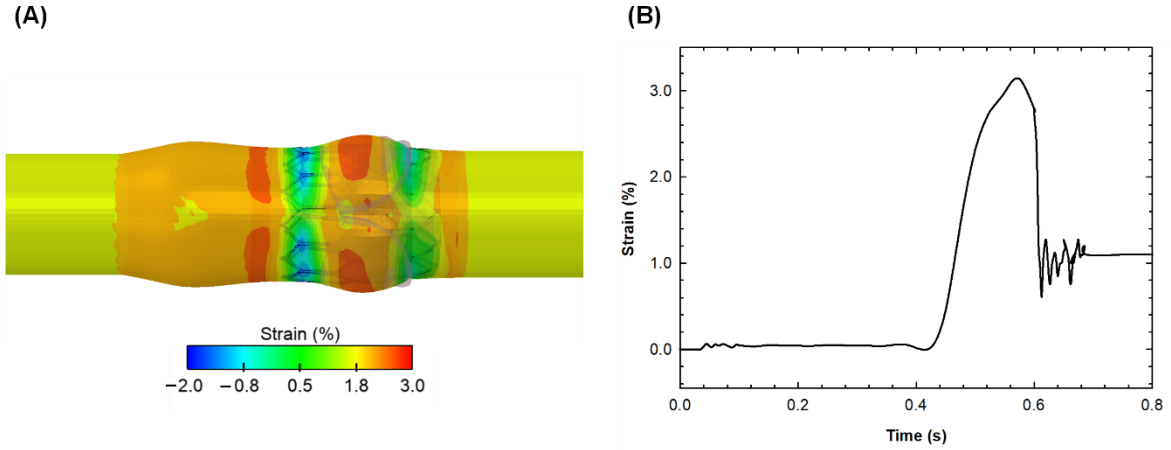

*Figure 4.5 Contour plot of circumferential engineering strain felt by the vessel (**A**) and strain (%) as a function of time of the polymer optical fiber (**B**).*

Figure 4.6 presents the PTT change estimates for various distances between PPG sensors and PWV with the pressure gradient across the bioprosthesis. It is evident that the pressure gradient across the bioprosthesis significantly affects the PWV estimates. Specifically, as the pressure gradient rises, the PWV estimates also increase. This relationship is explained by the Bramwell–Hill equation (Equation (2)), which indicates that PWV is proportional to the square root of the pressure gradient. On the other hand, the PTT estimates vary with the distance between the PPG sensors. As the distance between the proximal and distal PPG sensors around the implanted device increases, the PTT estimates also rise.

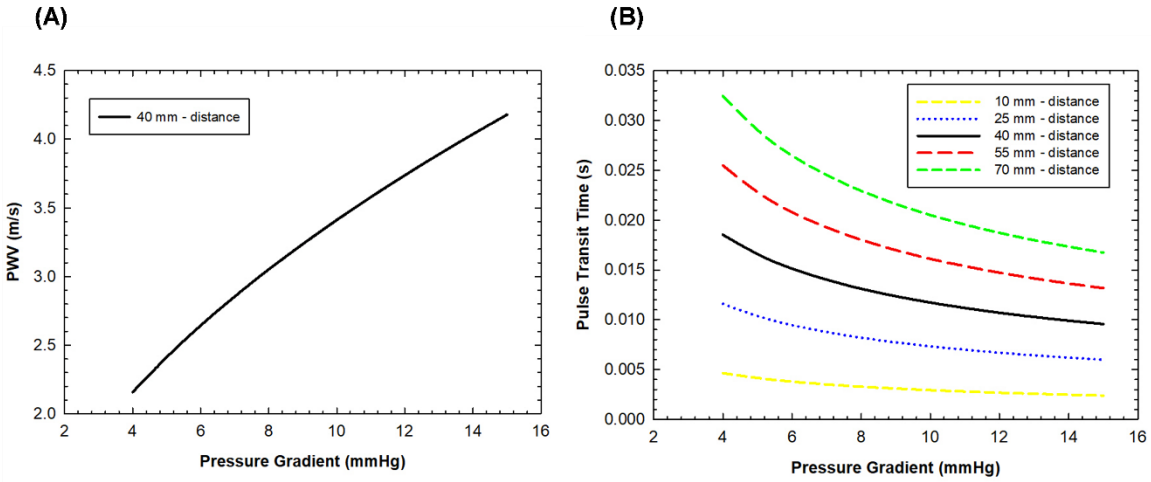

*Figure 4.6 Estimations of PWV for the optimal distance between the PPG sensor (40 mm) (**A**) and estimations of PTT for different distances between PPG sensors (**B**) as a function of the transvalvular pressure gradient.*

4.5 Discussion and Conclusion

This chapter presented a multiphysics computational framework for the analysis of fluid–structure interaction in an idealized model of a vessel containing a balloon-expandable THV. The goal was to estimate structural and hemodynamic parameters — flow velocity, blood pressure, and vessel wall deformation — necessary for the sizing of optical and PPG sensors for monitoring prosthetic function.

The simulations showed that the highest values of circumferential deformation are found at the level of the Valsalva sinuses. However, this location might not be ideal for estimating vessel deformation, as the natural curvature of the sinuses can introduce bending effects on the fiber that affect its measurement. The optimal position for placing the polymer optical fiber is therefore in the distal region, about 1 cm below the sinotubular junction, where post-TAVI circumferential deformations remain high while minimizing bending effects on the fiber. Following the multiphysics simulations, the predicted circumferential deformation (about 3%) is consistent with the aortic distensibility patterns documented in the literature for elderly subjects [133], and with the principal strain values observed by Satriano et al. [134] in patients undergoing TAVI. The strain estimates obtained through FSI simulations are also compatible with the full measurement range achievable with polymer or Bragg grating optical fiber sensors.

With regard to PPG sensors, the analysis demonstrated the effectiveness of positioning the sensors upstream and downstream of the bioprosthesis for measuring the transvalvular pressure gradient. However, positioning in the proximal region presents critical issues due to the intrinsic anatomical constraints of the aortic root and the left ventricular outflow tract. From the parametric analysis of the distance between the PPG sensors, it emerged that the optimal distance is 70 mm; however, such a distance could cover almost the entire length of

the aorta and left ventricular outflow tract. Reducing the distance to 40 mm represents a more realistic compromise between measurement accuracy and anatomical constraints.

Several sensor-based approaches have been proposed in the literature for monitoring valvular prostheses. Bailoor et al. [88] employed pressure sensors integrated into the stent frame, combined with machine learning techniques to classify healthy and pathological valves. Vennemann et al. [12] proposed magnetic sensors for measuring transvalvular flow, while Marcelli et al. [10] used electrical impedance measurements with electrodes integrated into mechanical valves. However, these technologies require the integration of active components within the implanted device, subject to stricter engineering and regulatory standards compared to wearable devices. Unlike existing approaches, the framework developed in this chapter combines PPG sensors and optical fibers with analytical considerations of PWV and PTT for estimating the transvalvular pressure gradient, integrating for the first time multiphysics FSI analysis with the design of non-invasive, low-cost sensors for monitoring THV functionality.

The study presents several limitations, including the use of an idealized vascular geometry that does not capture patient-specific anatomical variability and the adoption of linear elastic material properties for the aortic wall and valve leaflets. Furthermore, the natural curvature of the human aorta, in contrast to the straight ideal model used here, could influence the deformation field in the circumferential direction. Analyzing the sensitivity of the proposed sensors to these geometric variations could help identify regions of the aortic wall with critical deformations, further improving model development. The investigation was also conducted exclusively through numerical simulations, without direct comparison to experimental data. Nevertheless, the concept outlined in this study aims to demonstrate how multiphysics in-silico simulations can be used to optimize sensor integration in an in-vitro aortic model. This approach appears promising for improving the evaluation of THVs —

devices with an expected lifespan of about five years — particularly in identifying degeneration of biological leaflets and developing strategies for timely prophylactic intervention.

The next step in developing this approach involved comparing numerical predictions with experimental data, a fundamental aspect for verifying the consistency of computational estimates of PWV and PTT with measurements acquired under controlled conditions. The following chapter will focus on the design and development of an in vitro experimental setup, employing PPG sensors on a 3D-printed aortic phantom within a mock loop system, with the aim of consolidating the proposed framework and evaluating its applicability in scenarios representative of physiological hemodynamic conditions.

Chapter 5

5. From Numerical Markers to Experimental Measurement: Testbench and Protocol Design

This chapter presents a preliminary numerical-experimental comparison aimed at verifying the consistency between computational predictions and corresponding physical measurements. The flow results obtained from the FSI analysis were used to develop an analytical estimate of the metrics derived from the PPG signal, namely the pulse transit time (PTT) and the pulse wave velocity (PWV). These estimates were compared with the corresponding experimental measurements, which were obtained by replicating the boundary conditions of the numerical simulation in an in vitro setup using a 3D-printed aortic phantom within a mock circulatory loop. The goal of this comparison is to quantify the discrepancy between the two methodologies and provide a preliminary assessment of the consistency of the computational model for the purpose of sensor design. The results of this study have been published in [135].

5.1 Analytical Estimation of PPG Metrics from FSI Simulation

The MATLAB script developed in Paragraph 4.3 was used for the analytical estimation of PWV and PTT metrics. The analytical model, based on the Bramwell–Hill equation, relates the transvalvular pressure gradient, the distance between the sensors, and the PWV, as described in Chapter 4. The PTT is calculated as the ratio between the distance between the PPG sensors and the PWV. The values of pressure gradient and vessel area used in the calculation were extracted from the post-TAVI FSI simulation. In this case, unlike the parametric analysis conducted in the previous chapter, a single distance between the PPG

sensors of 70 mm was considered, corresponding to the configuration adopted in the experimental setup described in the following paragraphs. The transvalvular pressure gradients considered are in the range from 4 to 15 mmHg.

5.2 3D Printed Model and Mock Circulatory Loop

A flexible aortic model was created using stereolithography 3D printing technology with Formlabs' elastic 50 A resin (Formlabs, Somerville, MA, USA). This resin demonstrated a tensile rupture strength of 3.4 MPa and an elongation at rupture of 160%, which are properties comparable to soft tissue [136]. The aortic model was produced using the Form 3B + system (Formlabs, Somerville, MA, USA) with a layer thickness of 50 µm. After printing, the model was washed in isopropyl alcohol for 30 minutes and then cured under UV light for another 30 minutes. The dynamic flow loop included silicone tubing, plastic connectors, a custom pulsatile pump, the 3D aortic model, a compliance chamber, pressure and PPG sensors, and a fluid collector (Figure 5.1).

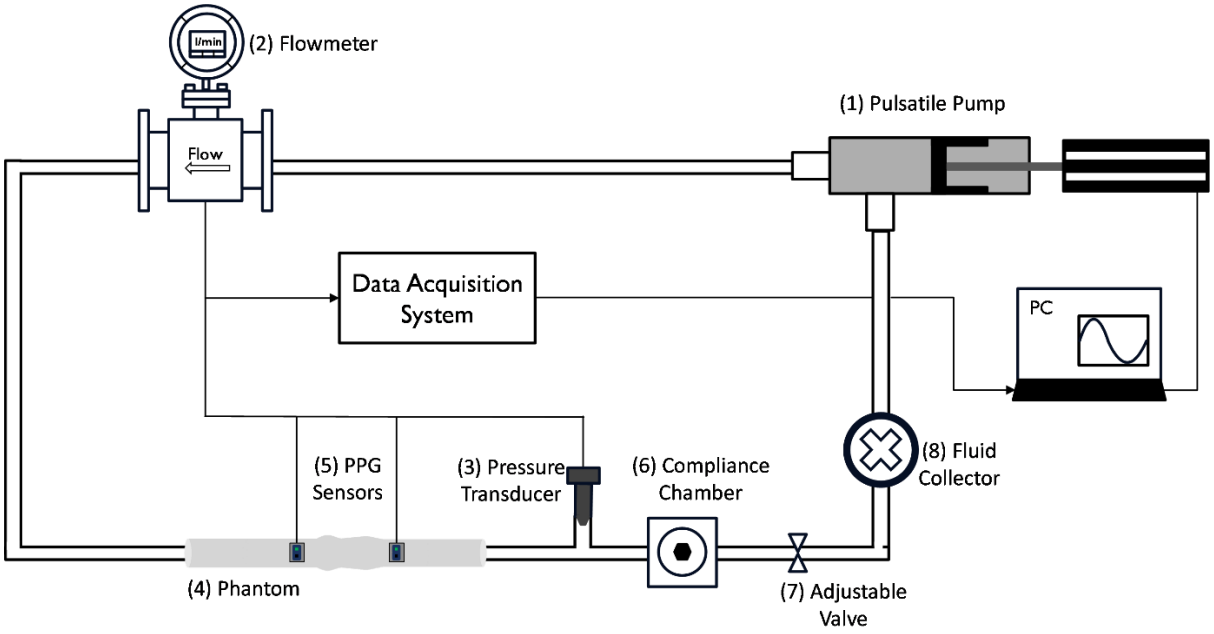

Figure 5.1 Schematic of the mock circulatory loop: (1) pulsatile pump, (2) flowmeter, (3) pressure transducer, (4) 3D-printed aortic phantom, (5) PPG sensors, (6) compliance chamber, (7) adjustable valve, (8) fluid collector.

The pumping mechanism featured a brushless linear actuator (P01-48x360F; LinMot, Spreitenbach, Switzerland) with a piston head to control the stroke motion. The compliance chamber was equipped with a spring-mounted piston and adjustable spring rate to simulate the Windkessel effect [136]. For simplicity, water was used as the perfusion fluid. Valve resistance was employed to modify fluid pressure, while the pump stroke controlled the flow. An electromagnetic flowmeter (Optiflux 5300C; Krohne, Duisburg, Germany) was installed on the plastic tube after the pulsatile pump to measure flow. Similarly, fluid pressure was gauged using a pressure transducer (X5072 Druck; GE Measurement & Control, Italy) connected after the aortic wall model. PPG data were gathered from two PPG sensors (DFRobot, China) operating at a 520 nm wavelength and positioned on the outer surface of the aortic model. The sensors were placed 70 mm apart. Both PPG signals were captured using a C Series DAQ Ethernet chassis (CDAQ-9181, National Instruments, USA) for real-time acquisition and visual analysis via LabView software (National Instruments, Austin, TX, USA). A baseline hemodynamic condition was set using a physiological flow waveform with a systemic pressure of 120/80 mm Hg, a systolic duration of 300 ms, a cardiac output of 4.7 L/min, and a heart rate of 70 beats/min. Measurements were taken three times for 5 minutes each during the experiments.

5.3 Experimental Data Analysis

A computational script was developed within the MATLAB mathematical computing environment (The MathWorks Inc., MA, USA) to estimate the Pulse Transit Time (PTT) and Pulse Wave Velocity (PWV) using two photoplethysmography (PPG) sensors. This script is designed to load data and define relevant variables and parameters necessary for subsequent analyses, including the inter-sensor distance, vessel diameter, vessel wall thickness, fluid density, and a sampling frequency of 5000 Hz. The script is programmed to identify pairs of peaks within the PPG signals. The heart rate is computed based on the number of detected

peaks and the total duration. The PTT is calculated as the absolute difference between the times of corresponding peaks in the two PPG signals [137], while the PWV is determined as the ratio of the distance between the PPG sensors to the PTT.

5.4 Results

Figure 5.2 presents the estimated values of Pulse Wave Velocity (PWV) and Pulse Transit Time (PTT) for a Photoplethysmography (PPG) sensor distance of 70 mm, depicted as a function of the pressure gradient across the bioprosthesis. An increase in the pressure gradient across the bioprosthesis corresponds to an increase in PWV estimations. Conversely, PTT estimates decrease as the pressure gradient across the device diminishes. With a numerically predicted pressure gradient of 5.7 mmHg, the analytical solution provides a PTT of 26 ms and a PWV of 2.7 m/s.

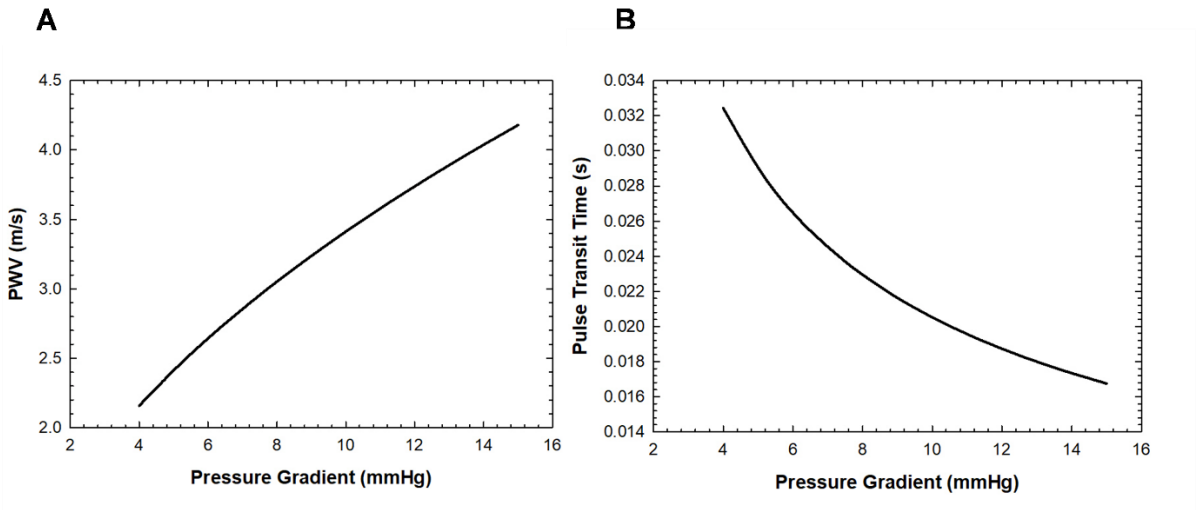

*Figure 5.2 Estimations of PWV (**A**) and estimations of PTT (**B**) as a function of transvalvular pressure gradient both for the optimal distance between PPG sensor (70 mm).*

Figure 5.3 displays the profiles of PPG signals for two cardiac cycles, highlighting an observable delay of the distal PPG sensor relative to the proximal PPG sensor. This delay corresponds to the PTT among PPG signals and is measured to be 24.63 ms. The PWV was

determined to be 3.14 m/s. Consequently, the relative errors between predictions and experimental results were 7.7% and 20.5% for the PTT and PWV, respectively.

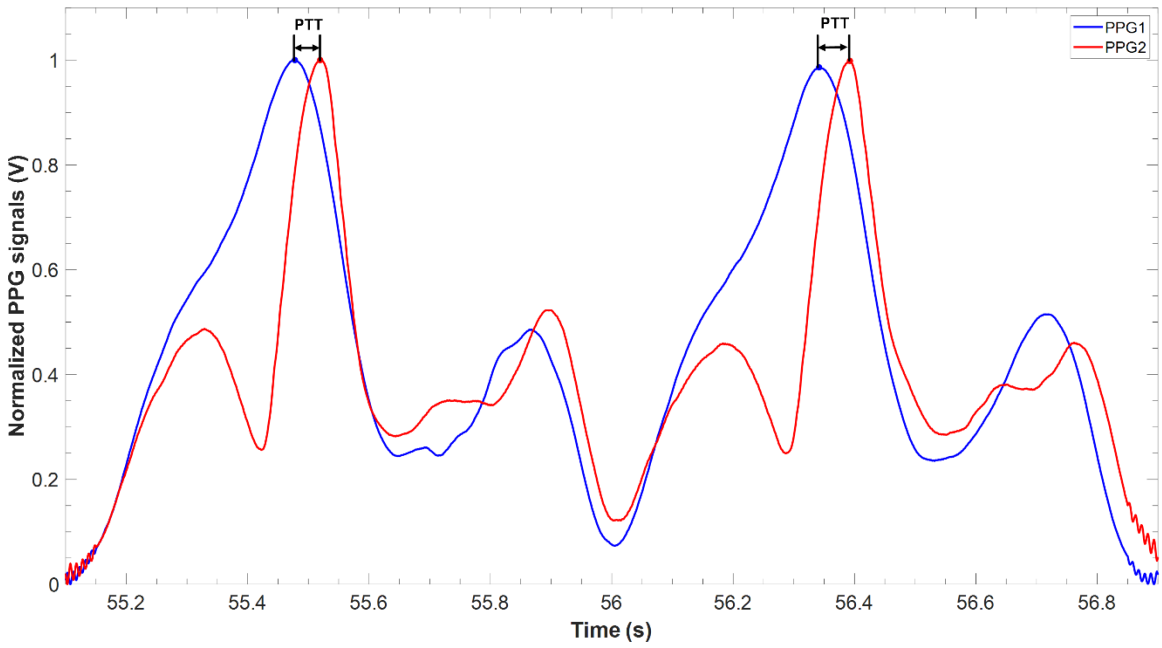

Figure 5.3 Two pulses from signal of proximal PPG 1 and distal PPG 2 from two cardiac cycle.

5.5 Discussion and Conclusion

The context of this chapter lies in the need to verify the consistency of computational predictions with physical measurements, an essential step to consolidate the sensor design framework introduced in Chapter 4. Indeed, the numerical-experimental comparison represents a fundamental requirement for evaluating the applicability of the computational model in scenarios that represent real hemodynamic conditions.

In the literature, few studies have integrated both the numerical and experimental components in the design of sensorized systems for valve monitoring. Among these, Vennemann et al. [89] and Naccarata et al. [92] have combined numerical simulations with in vitro experimental tests, albeit focusing on active implantable technologies. In contrast,

the present study proposes, for the first time, a numerical-experimental comparison based on non-invasive PPG sensors positioned on the external surface of the vascular model.

The numerical-experimental comparison presented in this chapter enabled an initial assessment of the consistency between the analytical predictions derived from the FSI simulation and the corresponding in vitro measurements. The relative error between the predicted and experimental values of PTT was 7.7%, while for PWV the error increased to 20.5%. This discrepancy can presumably be attributed to various factors, including differences in the mechanical properties of the materials and pressure conditions between the numerical model and the experimental setup. In particular, the computational model assumes linear elastic properties for the aortic wall, while the 3D-printed silicone phantom exhibits a different mechanical response, which can influence the propagation of the pressure wave and, consequently, the estimation of the PWV.

It should also be noted that the 70 mm distance between the PPG sensors, although identified as optimal by the parametric analysis in Chapter 4, covers a significant portion of the length of the aorta and the left ventricular outflow tract. Furthermore, the relatively high error observed in PWV may be partly attributable to the reduced distance between the sensors. Supporting this hypothesis, the study by Diana et al. [138], conducted using the same type of PPG sensors and a similar experimental setup on silicone phantoms, demonstrated that the optimal placement of the sensors is at a distance of 150 mm, and that shorter distances compromise the accuracy of PWV estimation. Based on this evidence, in Chapter 6 the distance between the PPG sensors was increased to improve the reliability of the measurements.

Despite the observed discrepancies, the numerical-experimental comparison conducted in this chapter demonstrated that the analytical predictions derived from the FSI simulation are consistent with the in vitro measurements, particularly regarding the estimation of PTT. This

represents a positive initial indication of the computational model's ability to reproduce the physical behavior of the system, although the differences found in PWV suggest the need for further investigation. However, the comparison was carried out by experimentally replicating only a single operating condition, contrasting the analytical estimates of PPG metrics obtained from numerical simulations with the corresponding measurements of PTT and PWV acquired via physical PPG sensors. To overcome these limitations, Chapter 6 will significantly extend the experimental campaign through the use of a Latin Hypercube Sampling-based experimental design to generate multiple hemodynamic scenarios and will introduce machine learning techniques for predicting and classifying valve performance based on the PPG signals acquired in vitro.

Chapter 6

6. Non-Invasive Monitoring of Transcatheter Heart Valve Using Photoplethysmography and Machine Learning

With the extension of TAVI to younger patients with a longer life expectancy, the need for continuous and non-invasive monitoring of the implanted device outside the hospital setting is becoming increasingly relevant. However, correlating non-invasive physiological metrics—such as pulse transit time (PTT) and pulse wave velocity (PWV)—with indicators of device performance, such as the geometric orifice area (GOA), remains an open challenge, especially due to the wide variability of patients' hemodynamic conditions.

This chapter explores the feasibility of monitoring the functionality of a transcatheter heart valve (THV) by combining the acquisition of photoplethysmographic (PPG) signals with machine learning techniques. An in vitro experimental setup was developed, based on a mock circulatory circuit with an Evolut FX device implanted in a compliant aortic phantom, and a large dataset of hemodynamic scenarios was generated using Latin Hypercube Sampling. Metrics derived from the PPG signals, together with hemodynamic variables, were used to train a linear regression model with polynomial features and a threshold-based classifier, with the aim of estimating the GOA and classifying leaflet mobility as physiological (HLM) or reduced (RLM), providing a proof-of-concept for the early detection of bioprosthesis deterioration. The contents of this chapter are based on the work published in Puleo et al. [139].

6.1 Methods

The methodology commenced with an assessment of transcatheter heart valve (THV) performance across various hemodynamic scenarios, followed by the development of a machine learning regression model to predict valve performance utilizing flow and photoplethysmography (PPG)-related metrics. The self-expandable Evolut FX (Medtronic, USA) device was deployed within a phantom model equipped with two PPG sensors on its surface, and the valve area was optically measured under diverse hemodynamic conditions. Consequently, the flow variables and measured valve areas were employed to implement a machine learning model for the regression and classification of the peak opening of valve leaflets.

6.2 Design of Experiments

The in vitro flow plan was developed utilizing Latin Hypercube Sampling, which entailed varying the pump stroke volume, heart rate, and systolic and diastolic pressures by twice the standard deviation from reference values. Ten combinations of hemodynamic variables were employed to generate 40 distinct flow scenarios (4 flow variables × 10 random input combinations). Given that the sampling methodology could yield implausible combinations of flow variables, non-physiological conditions were identified and excluded from the experiments.

Flow combinations with a systolic-to-diastolic pressure drop of ≤ 20 mmHg or higher were omitted. Table 2 presents the nominal values and boundaries for the flow variables.

Table 2. Nominal values together with lower and upper bounds of the flow variables used for Latin Hypercube Sampling.

	Nominal	Lower Bound (-2 σ)	Upper Bound (+2 σ)
Stroke Volume (mL/beat)	64	45	90
Heart Rate (bpm)	70	51	100
Systolic Pressure (mmHg)	120	95	180
Diastolic Pressure (mmHg)	63	60	100

6.3 Mock Loop and PPG Sensor

The flow performance of the 23-mm self-expandable Evolut FX device was evaluated using a compliant phantom model, as detailed in a prior study [140]. The silicone phantom was engineered to replicate the aortic anatomy of a patient who had undergone endovascular repair. The inlet aortic root was sufficiently extended, allowing for manual placement of the THV with the last cell row oriented towards the left ventricular outflow tract and the remainder positioned in the aortic root.

A custom-designed mock-circulatory loop was employed to quantify the device's performance [141]. Although the reliability of the mock loop was not formally tested in the current study, the system was designed to simulate a wide range of hemodynamic scenarios by adjusting pump stroke volume, systemic resistance, and compliance chamber settings, as demonstrated in previous publications [140, 141]. Specifically, the flow loop comprised a pulsatile pump, the phantom model with the THV device and PPG sensors, the compliance chamber, and the fluid collector, all interconnected by silicone tubes and plastic connectors (Figure 6.1).

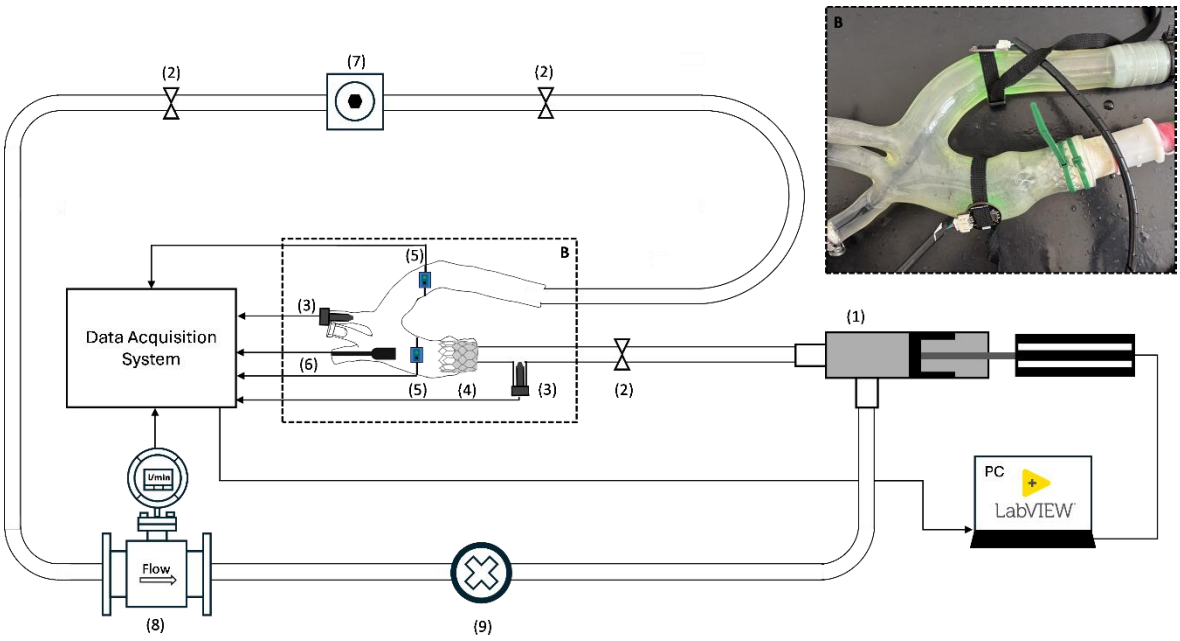

*Figure 6.1 (**A**) Mock circulatory loop showing 1) the pulsatile pump, 2) adjustable valves, 3) pressure sensors, 4) THV device, 5) PPG sensors, 6) endoscopic camera, (7) compliance chamber, (8) electromagnetic flowmeter, (9) fluid collector; (**B**) photograph of the phantom model with device and attached PPG sensors.*

The pumping system included a brushless linear actuator (P01-48x360F, LinMot, CH) capable of moving a piston within a cylindrical steel chamber. An electronic controller could displace the piston to any prescribed stroke, and the resulting displacement was used to calculate the fluid stroke volume. The piston was actuated using a sinusoidal waveform with a duration corresponding to the desired heart rate, assuming a systolic duration of one-third of the cardiac cycle. A valve was installed in the pumping head to mimic the mitral valve, permitting fluid flow into the piston chamber from the fluid collector. The compliance chamber utilized a spring-mounted piston and an adjustable spring to regulate the pressure drop in the mock loop. Adjustable valves were also positioned proximally and distally to the compliance chamber to calibrate systemic pressure based on the flow scenarios described in the experimental design. Water was used as a blood-analogous fluid.

Fluid pressure was measured with two pressure transducers (X5072 Druck, GE Measurement & Control, USA) placed before the aortic phantom and in the left subclavian artery. Flow measurements were conducted using an electromagnetic flowmeter (Optiflux

5300C, DE). Pressure and flow were measured and visualized in real-time using a LabView application (v2021, National Instruments, USA). For THV imaging during cardiac cycles, an endoscopic camera was inserted along the phantom brachiocephalic artery and the distal ascending aorta. Images were acquired with the camera positioned normal to the valve plane at a frame rate of 30 fps, using a ruler behind the valve for accurate scaling. Two PPG sensors (DFRobot, CH) with a wavelength of 520 nm were attached to the outer surface of the aortic phantom using elastic bands. One PPG sensor was placed at the mid-height of the ascending aorta, and the other was attached to the descending aorta (Figure 6.1B). Both PPG signals were acquired in real-time using a C Series DAQ ethernet chassis (CDAQ-9181, NI, USA) with a sampling frequency of 5 kHz.

6.4 PPG Metrics and Valve Performance

Photoplethysmographic (PPG) signals and valve leaflet motion were analyzed using Matlab (v2024, MathWorks, USA). The PPG signals underwent bandpass filtering with a frequency range of 0.5 to 5 Hz. A peak-to-peak detection algorithm was employed to determine the temporal distance between signal peaks from the sensors. Starting from the peak time of the filtered signals, the pulse wave velocity (PWV) was calculated according to Eq. 3, introduced in Chapter 2, as the ratio between the distance d between the PPG sensors along the centerline of the vessel, as determined in the computer-aided design model of the phantom, and the pulse transit time (PTT) measured as the time interval between the corresponding peaks of the two PPG signals.

Endoscopic images were employed to estimate the geometric orifice area (GOA) at the systolic peak of each cardiac cycle. Initially, images were converted to grayscale, and adaptive histogram equalization was applied to enhance image quality. The valve area was manually delineated using a spline curve, and an active contour algorithm was utilized to

refine the boundary of the free edges of THV leaflets. The GOA in pixels was calculated and subsequently converted to square millimeters.

For each hemodynamic scenario, 10 cardiac cycles were recorded to compute 10 PTT, PWV, and GOA values. This approach allowed for the expansion of inputs for machine learning to approximately 400 data points.

6.5 Machine Learning

A predictive model for GOA was constructed utilizing four flow variables and two PPG-related metrics. Prior to model training, the dataset underwent preprocessing to eliminate outliers from both the model features (i.e., flow and PPG variables) and the model output (i.e., GOA). Specifically, outliers were identified and removed using the interquartile range (IQR) method, which excludes values that fall beyond 1.5 times the IQR from the first and third quartiles for both input features and GOA. The features were then normalized using min–max scaling. Consequently, a linear regression model incorporating second-order polynomial and interaction features was developed to predict GOA values.

The model used six input features, including four flow-derived variables, namely stroke volume, heart rate, systolic pressure and diastolic pressure, as well as two PPG-derived metrics, PTT and PWV. These features were expanded through a second-order polynomial transformation that included quadratic and pairwise interaction terms. Denoting the normalized input features as x_1, …, x_6, the predicted geometric orifice area was expressed as:

$$\widehat{GOA} = \beta_0 + \sum_{i=1}^{6} \beta_i x_i + \sum_{i=1}^{6} \beta_{ii} x_i^2 + \sum_{i<j} \beta_{ij} x_i x_j \qquad \text{Eq. 10}$$

where β_0 is the intercept, β_i are the linear coefficients, β_{ii} the quadratic coefficients, and β_{ij} the pairwise interaction coefficients. The second-order expansion of the six features results

in 27 polynomial terms (six linear, six quadratic, and fifteen interaction terms) in addition to the intercept. The coefficients were estimated by ordinary least squares, and the dataset was divided into 80% for training and 20% for testing.

Following regression, a threshold-based classification was applied to the predicted GOA values to categorize them into healthy leaflet motion (HLM) and reduced leaflet motion (RLM). A pressure gradient ranging from 24–40 mmHg and GOA ranging from 170–230 mm^2 were assumed for the classification of HLM conditions, as these parameters are commonly employed to assess valve performance in echocardiography [54]. To evaluate classification performance, class labels derived from predicted GOA values were compared to ground truth labels based on measured GOA and pressure gradient values.

Model performance was quantified using R-squared, root mean squared error (RMSE), mean absolute error (MAE), and a confusion matrix. Additionally, statistical analysis was conducted to compare the actual and predicted GOA values in the test set. After assessing normality using the Shapiro–Wilk test, a paired Wilcoxon signed-rank test was performed to evaluate potential statistical differences between the actual and predicted GOA values.

6.6 Results

Figure 6.2 presents representative interactions among flow variables derived from the random sampling methodology.

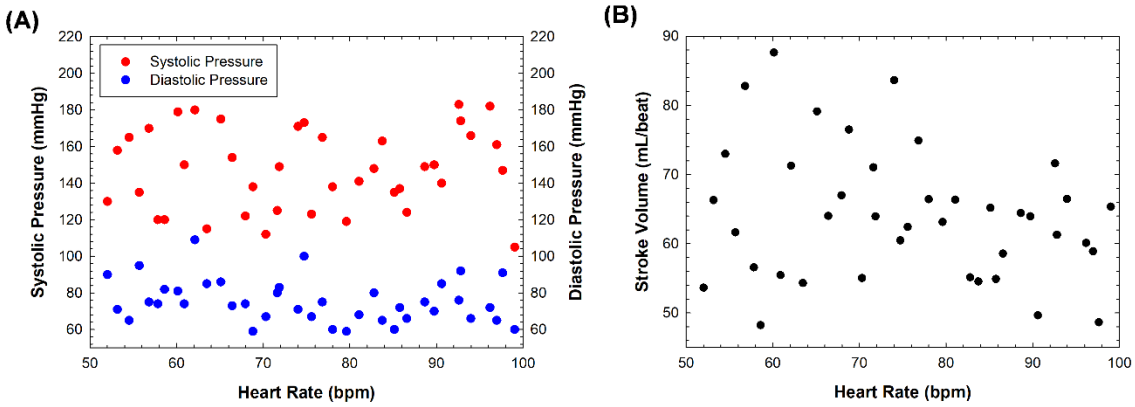

*Figure 6.2. Latin Hypercube Sampling of flow variables showing the variation of (**A**) systolic and diastolic pressure versus the heart rate, and (**B**) stroke volume versus the heart rate.*

Each variable range was uniformly sampled, resulting in a well-distributed projection of samples on each axis. The experiments were designed to maximize the diversity of input flow variables and minimize the risk of omitting critical areas of the input space.

The measured profiles of fluid pressure over the cardiac cycle varied depending on the combined effect of flow variables (Figure 6.3A–C).

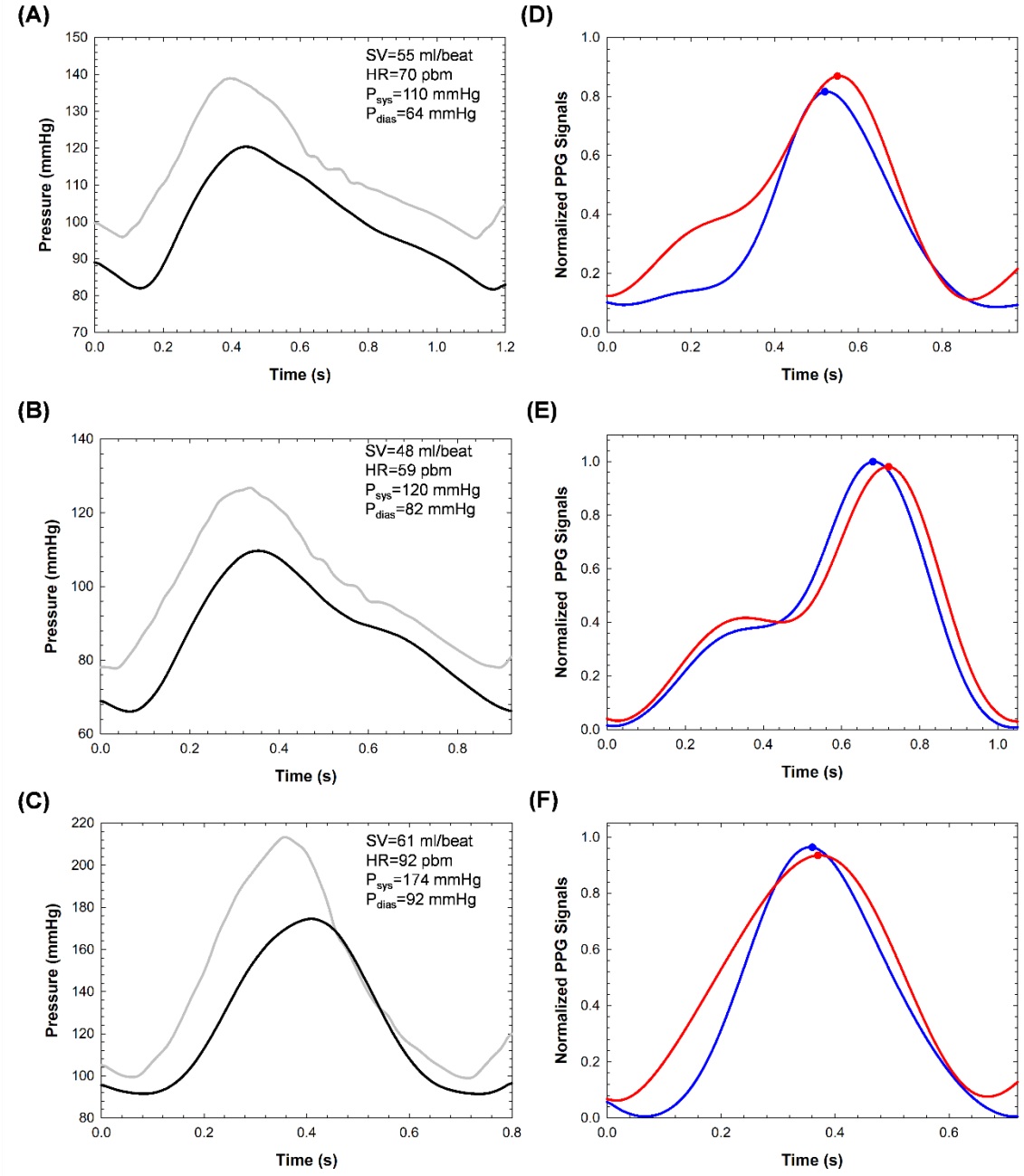

*Figure 6.3 (**A-C**) Fluid pressure measurements at the inlet (grey line) and left subclavian artery (black line) for different flow scenarios and (**D-F**) corresponding PPG signals for three hemodynamic scenarios representing hypotensive (top), normal (middle), and hypertensive (bottom) flow conditions; the red and blue curves show PPG signals of sensors in the ascending and descending aorta, respectively; dots show peaks computed by the detecting algorithm; Note: SV = stroke volume, HR = heart rate; P_{sys} = systolic pressure; P_{dias} = diastolic pressure.*

Figure 6.3D–F displays the signals from two PPG sensors positioned along the aorta at a distance of 143.0 mm. Across all experiments, the PTT ranged from 10.8 to 105.9 ms, and the PWV values ranged from 1.4 to 13.7 m/s.

Similarly, Figure 6.4 illustrates the device valve opening as measured by the GOA under three representative hemodynamic conditions. For the proposed flow plan, the GOA ranged from 159.5 to 239 mm².

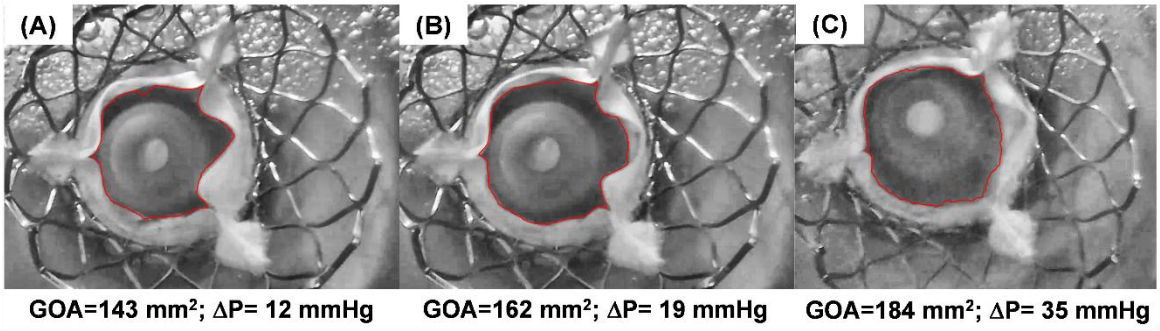

*Figure 6.4. Representative photograph of THV leaflet opening with the GOA (red line) for three hemodynamic scenarios representing (**A**) hypotensive, (**B**) normal, and (**C**) hypertensive flow conditions.*

The linear regression model achieved an R^2 of 0.83, RMSE of 7.18, and MAE of 5.58. The plot of predicted versus actual values of GOA indicates a strong fit (Figure 6.5A). The normality assumption was not satisfied for both predicted and actual GOA values, and the paired Wilcoxon signed-rank test revealed no significant difference between predicted and actual GOA values ($p = 0.144$ and alpha > 0.05). The threshold-based classification applied to the predicted GOA values, categorizing them into HLM and RLM, demonstrated a classification accuracy of 95%, with a sensitivity of 100% for detecting HLM and a specificity of 91% for identifying RLM cases (Figure 6.5B).

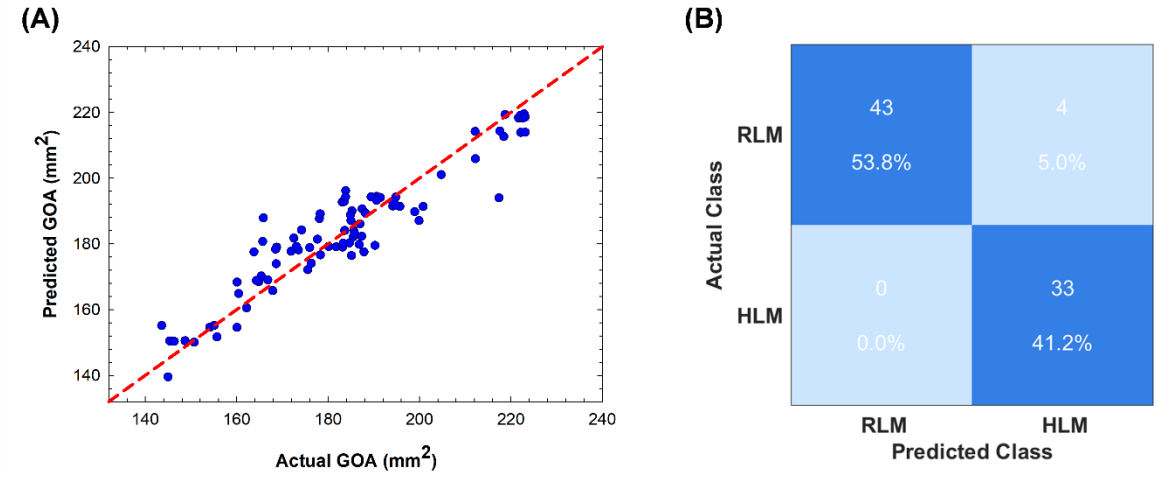

*Figure 6.5 (**A**) Scatter plot comparing predicted GOA values from the linear regression model with actual experimental GOA values; (**B**) confusion matrix showing the classification performance of the threshold-based model in distinguishing HLM versus RLM.*

6.7 Discussion

This study explored the feasibility of non-invasive monitoring of THV performance through the acquisition of photoplethysmographic signals and machine learning algorithms. Starting from a dataset of hemodynamic scenarios generated via Latin Hypercube Sampling, an experimental framework was developed that combines the acquisition of PPG signals with regression and classification models for estimating the geometric orifice area (GOA) and categorizing leaflet mobility. The most significant result is the classifier's ability to identify the presence of a compromised opening area, which likely reflects the onset of leaflet degeneration. This aspect is relevant because the durability of THVs is an essential requirement for expanding structural cardiac procedures to younger populations. Future developments of the proposed technological solution may enable personalized monitoring of prosthetic function for the early detection of adverse events and the management of patient follow-up after TAVI procedures.

For all the hemodynamic scenarios examined, the results confirmed the presence of a detectable variation in GOA based on PPG signals acquired at two different anatomical sites. The statistical distribution of entry points enabled effective and efficient experimental

planning, although the random sampling methodology may not have covered all possible interactions among flow variables. The distance between the PPG sensors is the most influential factor in measuring PTT and PWV parameters. Although not specifically investigated in this study, the inter-sensor distance along the longitudinal direction of the aortic phantom was chosen based on previous research that analysed the sensitivity of silicone materials and the PPG sensors' distance on resulting PTT and PWV parameters [138]. Specifically, PPG sensors do not provide reliable measurements for distances less than or equal to 100 mm, as the error on PWV can reach up to 30% compared to a distance of about 150 mm.

In contrast to Chapters 4 and 5, where sensors were strategically positioned upstream and downstream of the valve to directly estimate the transvalvular pressure gradient, the current study employs a different configuration. Both sensors are placed downstream of the device, one on the ascending aorta and the other on the descending aorta, separated by a distance of 143 mm along the vessel's centerline. This arrangement facilitates an aortic PWV estimate with a level of accuracy appropriate for training the machine learning model. Although this configuration does not directly measure the transvalvular gradient, recent literature supports the hypothesis that the pulse wave propagating downstream of the valve contains valuable information regarding valvular function. Wilson et al. [142] conducted an in silico study utilizing a database comprising over 16,000 virtual subjects, demonstrating that a reduction in the valvular orifice area induces significant alterations in the pulse wave morphology. These changes are evident both in the ascending aorta, characterized by a more rounded flow wave and a diminished peak, and in peripheral sites, where strong correlations were observed between the severity of stenosis and various indices derived from the pulse wave. This finding suggests the potential application of these observations for the early diagnosis and monitoring of aortic stenosis. Similarly, Plunde et al. [143] reported that following valve replacement for aortic stenosis, the morphology of the brachial pulse wave transitions from

a prolonged and flattened pattern, indicative of *pulsus parvus et tardus*, to a steeper systolic upstroke. This confirms that valvular function exerts a direct influence on the characteristics of the wave measured at a distance from the valve. Terentes-Printzios et al. [70] documented a notable increase in carotid-femoral PWV immediately following TAVI, rising from 7.5 to 8.4 m/s, a change that persisted one year post-procedure. This finding illustrates that the alleviation of stenosis alters the propagation of the pulse wave within the aorta. The evidence suggests that aortic PWV, although not a direct measure of the transvalvular gradient, is responsive to alterations in valvular function. In the current study, this indirect information was derived using a machine learning model, which, by integrating PPG metrics with hemodynamic variables, is capable of identifying non-linear relationships that are not discernible through simple bivariate correlation analysis.

Despite the clinical need to monitor the structural deterioration of heart valves, few studies have attempted to develop in situ systems for valve prostheses. As discussed in Chapters 3 and 4, magnetic sensors [12], transvalvular impedance measurements [14], and pressure sensors integrated into the stent frame [88] have been proposed for monitoring device function. However, these technologies require the generation of an external electric field or miniaturization compatible with the thin metal structure of the THV stent, posing significant barriers to clinical translation. Differently, the present study proposed indirect measurements of THV function using low-cost PPG sensors combined with advanced signal processing. Moreover, among the cited studies, only Vennemann [89] and Bailoor et al. [13, 88] integrated machine learning techniques in their approach to valve monitoring. Vennemann developed an anomaly detection framework based on an unsupervised algorithm (one-class SVM) applied to implantable magnetic sensor data, demonstrating the ability to detect various degrees of aortic regurgitation in vitro; however, the approach is limited to identifying deviations from reference behavior without classifying the type of defect or providing a quantitative estimate of valve function. Bailoor et al., on the other hand,

employed a supervised approach using computational simulations to generate pressure signals and train leaflet mobility classification models, but the approach relies entirely on in silico data and on active sensors integrated within the device. Unlike both studies, the present work combines, for the first time, a supervised learning approach with experimentally acquired data from non-invasive PPG sensors, enabling not only the classification of leaflet mobility (HLM vs RLM) but also a quantitative estimation of the GOA based on a dataset of real hemodynamic scenarios.

From a regression standpoint, the model developed in this study explained 83% of the variability in GOA values obtained from different hemodynamic scenarios. PWV and heart rate ranked among the most influential input variables in the model's predictions, based on standardized coefficients; however, a dedicated sensitivity analysis would be necessary to more rigorously determine their predictive capacity in valve evaluation. Regarding classification, the model erroneously identified only four RLM cases as healthy valve configurations, achieving an accuracy of 95%, a precision of 0.89, and a recall of 0.91. Analysis of these cases revealed that the misclassification occurred under flow conditions close to the limits of the threshold adopted to discriminate between normal and compromised valve function, suggesting that the classification error may be clinically acceptable.

The fact that the machine learning model relies on arterial pressure measurements from the mock loop should not be considered a limitation, as recent developments in wearable technology have demonstrated the feasibility of cuffless blood pressure measurement [144]. It is therefore reasonable to hypothesize that a combination of various physiological signals and PPG-derived metrics could be employed to predict device valve function without direct recourse to echocardiography or computed tomography.

6.8 Challenges and Future Directions

The present study has some limitations that must be considered when interpreting the results. The experimental design, characterized by the random division of data at the level of individual heartbeats, could introduce data leakage, since beats belonging to the same hemodynamic scenario share similar wave morphology and statistics. Although the model was trained and tested multiple times with different random splits to assess repeatability and demonstrated consistent performance, a more robust approach would require a scenario-level cross-validation strategy (leave-one-scenario-out) to more rigorously evaluate generalizability to unobserved physiological conditions. Furthermore, the classification of leaflet mobility was based on a posteriori thresholding of the predicted GOA values, using clinically inspired intervals that may not be fully applicable to the in vitro setup. This indirect approach may amplify regression errors. Future studies will be necessary to verify the reliability of the model on a broader set of hemodynamic scenarios and to validate effective thresholds for reduced leaflet mobility in both experimental and clinical conditions. The use of water as the working fluid, rather than blood or a solution that mimics its rheological properties, can influence viscosity-dependent parameters such as PTT and PWV, potentially generating relationships specific to the experimental setup. Therefore, the results are confined to an in vitro environment. As this study was conducted as a proof-of-concept, future research should focus on the technical implementation of the proposed monitoring solution and on strengthening methodological rigor to ensure reliable machine learning inference, generalizability of the model, and clinical applicability.

7. Conclusion and Outlook

This thesis has presented an integrated, multidisciplinary framework for the non-invasive monitoring of transcatheter heart valves (THV), addressing multiple levels of complexity—from computational design of sensor placement, through in vitro experimental testing, to the implementation of predictive models based on machine learning. As TAVI is progressively extended to younger and more diverse patient populations, the ability to continuously and non-invasively monitor the function of implanted biological devices becomes increasingly relevant to support long-term clinical management, enable early detection of valve deterioration, and ensure the safe expansion of transcatheter therapies.

The contributions of this thesis cover three main areas: multiphysics computational modeling for sensor placement design, comparison between numerical predictions and in vitro experimental measurements using PPG sensors, and the development of a proof-of-concept system based on machine learning for the automated prediction of valve functionality. Taken together, these developments constitute a coherent and progressive approach to the study and monitoring of THV performance.

Firstly, the thesis developed a multiphysics fluid-structure interaction (FSI) simulation to quantify the structural and hemodynamic parameters linked to the performance of a deployed THV in an idealized model of the aortic vessel. Analysis of circumferential deformation identified the optimal positioning of fiber optic sensors in a distal position relative to the sinotubular junction, minimizing bending effects. Furthermore, it was shown that PPG sensors positioned upstream and downstream from the bioprosthesis allow effective evaluation of the transvalvular pressure gradient. These results underscore the necessity of computational approaches to guide sensor design, a fundamental prerequisite for the development of low-cost monitoring systems aimed at detecting valve deterioration.

Secondly, numerical predictions were compared with experimental measurements through the development of an in vitro test bench based on a pulsatile mock circulatory loop and a compliant 3D-printed aortic phantom model. An analytical model based on the Bramwell–Hill equation was formulated to correlate pulse wave velocity (PWV) and pulse transit time (PTT) with the transvalvular pressure gradient. Experimental data showed good agreement with analytical estimates, with a relative error of 7.7% for PTT. This research demonstrates the feasibility and value of integrating numerical simulations and in vitro testing, where experimental feedback can reinforce computational indications and support the design of sensors for valve degradation monitoring.

Thirdly, the thesis developed a proof-of-concept system for the automated monitoring of THV performance by combining non-invasive PPG sensors and machine learning algorithms. Using a mock circulatory loop with a self-expanding Evolut FX THV, an experimental plan based on Latin Hypercube sampling generated a broad range of hemodynamic scenarios. Flow variables and metrics derived from the PPG signal were used to train regression and classification models able to predict the geometric orifice area (GOA) and to distinguish between normal and impaired valve function. The regression model achieved an R^2 of 0.83, an RMSE of 7.18 mm^2, and an MAE of 5.58 mm^2, while the classifier correctly identified leaflet reduced mobility with an accuracy of 95%, a precision of 0.89, and a recall of 0.91. These results demonstrate the feasibility of data-driven, sensor-based valve monitoring, representing a concrete first step toward the development of monitoring platforms capable of providing continuous functional assessment that goes beyond the limits of current periodic imaging-based follow-up strategies.

Overall, this thesis demonstrates that the integration of fluid-structure interaction simulations, in vitro experimental analyses, PPG sensor technology, and machine learning techniques can credibly, efficiently, and clinically complement current follow-up strategies

based on diagnostic imaging, supporting both improved long-term patient management and the development of new paradigms for non-invasive valve monitoring.

While the specific limitations of each contribution have been discussed in their respective chapters, some future development directions emerge across the work as a whole. On the computational front, extending FSI simulations to patient-specific geometries derived from clinical imaging would overcome the simplifications of the idealized model and bring numerical predictions closer to real anatomical scenarios. Experimentally, the adoption of blood-mimicking fluids and the expansion of investigated hemodynamic scenarios are necessary steps to strengthen the transferability of the results to the clinical context. Regarding the machine learning model, implementing scenario-level cross-validation strategies and defining clinically robust thresholds for leaflet mobility classification, through systematic comparison with echocardiographic data, are the next necessary steps to consolidate its predictive capability. Building on these developments, the translation of the proposed framework toward clinical use would require a progressive sequence of validation stages. A first step would consist of consolidating the in vitro evidence under testing conditions aligned with the verification and validation principles defined by ISO 5840-3 for transcatheter heart valve substitutes. A subsequent early clinical investigation in TAVI recipients, designed according to the good clinical practice framework of ISO 14155, would then allow the agreement between PPG-derived predictions and echocardiographic assessment to be evaluated in a real patient population, providing the evidence base needed for a broader clinical deployment of the proposed monitoring approach.

In conclusion, although challenges remain, the results of this thesis represent a significant advancement toward the development of non-invasive monitoring solutions for transcatheter heart valves, laying the groundwork for an evolution of current follow-up strategies toward a more continuous, functional, and patient-specific approach. Future work should focus on

addressing current limitations and broadening the applicability of this framework to a wider range of clinical scenarios, thereby improving patient management and sparking innovation in the field of transcatheter cardiovascular therapies.

8. List of Publications

Peer-reviewed Articles

1. Catalano C., Crascì F., **Puleo S.**, Scuoppo R., Pasta S., & Raffa G. M. (2024). Computational fluid dynamics in cardiac surgery and perfusion: A review. *Perfusion*, 40(2), 362–370. https://doi.org/10.1177/02676591241239277
2. **Puleo S.**, Pasta S., Scardulla F., & D'Acquisto L. (2024). Fluid-solid interaction analysis for developing in-situ strain and flow sensors for prosthetic valve monitoring. Sensors, 24(15), 5040. https://doi.org/10.3390/s24155040
3. Scuoppo R., **Puleo S.**, Sausa G., Cannata S., Gentile G., Guccione J. M., & Pasta S. (2025). Simulations of left atrial appendage inversion procedure: Patient-specific models with different appendage geometries. Computers in Biology and Medicine, 188, 109875. https://doi.org/10.1016/j.compbiomed.2025.109875
4. Diana G., Scardulla F., **Puleo S.**, Pasta S., & D'Acquisto L. (2025). Non-invasive estimation of arterial stiffness using photoplethysmography sensors: An in vitro approach. Sensors, 25(11), 3301. https://doi.org/10.3390/s25113301
5. **Puleo S.**, Diana G., Livolsi C., Nioi L., Cuscino N., Scardulla F., Pasta S., & D'Acquisto L. (2025). Non-invasive monitoring of transcatheter heart valve using photoplethysmography and machine learning. Artificial Organs. https://doi.org/10.1111/aor.70069

Conference papers

1. Diana G., Scardulla F., **Puleo S.**, Pasta S., & D'Acquisto L. (2024). A preliminary study on arterial stiffness assessment using photoplethysmographic sensors. Engineering Proceedings, 82(1), 80. https://doi.org/10.3390/ecsa-11-20455

2. **Puleo S.**, Diana G., Pasta S., Scardulla F., & D'Acquisto L. (2025). Sensor-based bioprosthetic valve monitoring: Numerical simulation and experimental design. In: Di Stefano, P., Gherardini, F., Nigrelli, V., Rizzi, C., Sequenzia, G., Tumino, D. (Eds.), Design Tools and Methods in Industrial Engineering IV. ADM 2024. Lecture Notes in Mechanical Engineering, pp. 44–51. Springer, Cham. https://doi.org/10.1007/978-3-031-76594-0_6
3. Otesteanu C., Diana G., Scardulla F., **Puleo S.**, Pasta S., D'Acquisto L., & Menon C. (2025). Machine learning for classifying vascular age using the second derivative of the PPG signal. 2025 6th International Conference on Communications, Information, Electronic and Energy Systems (CIEES). https://doi.org/10.1109/CIEES66347.2025.11300216

9. Bibliography

[1] Osnabrugge RLJ, Mylotte D, Head SJ, et al. Aortic stenosis in the elderly: Disease prevalence and number of candidates for transcatheter aortic valve replacement: A meta-analysis and modeling study. *J Am Coll Cardiol* 2013; 62: 1002–1012.

[2] Cribier A, Eltchaninoff H, Bash A, et al. Percutaneous transcatheter implantation of an aortic valve prosthesis for calcific aortic stenosis: first human case description. *Circulation* 2002; 106: 3006–3008.

[3] Attinger-Toller A, Ferrari E, Tueller D, et al. Age-Related Outcomes After Transcatheter Aortic Valve Replacement: Insights From the SwissTAVI Registry. *JACC Cardiovasc Interv* 2021; 14: 952–960.

[4] Blackman DJ, Saraf S, MacCarthy PA, et al. Long-Term Durability of Transcatheter Aortic Valve Prostheses. *J Am Coll Cardiol* 2019; 73: 537–545.

[5] Amat-Santos IJ, Messika-Zeitoun D, Eltchaninoff H, et al. Infective endocarditis after transcatheter aortic valve implantation: results from a large multicenter registry. *Circulation* 2015; 131: 1566–1574.

[6] Flores-Umanzor E, Nogic J, Cepas-Guillén P, et al. Percutaneous paravalvular leak closure after transcatheter aortic valve implantation: the international PLUGinTAVI Registry. *EuroIntervention* 2023; 19: E442–E449.

[7] Schaeffer T, Koechlin L, Jeger R, et al. Severe structural valve deterioration after TAVR with ACURATE Neo: report of two cases. *Front Cardiovasc Med*; 10. Epub ahead of print 2023. DOI: 10.3389/fcvm.2023.1135496.

[8] Morany A, Bardon RG, Lavon K, et al. Analysis of fibrocalcific aortic valve stenosis: computational pre-and-post TAVR haemodynamics behaviours. *R Soc Open Sci*; 11. Epub ahead of print 21 February 2024. DOI: 10.1098/rsos.230905.

[9] Ghosh RP, Marom G, Bianchi M, et al. Numerical evaluation of transcatheter aortic valve performance during heart beating and its post-deployment fluid-structure interaction analysis. *Biomech Model Mechanobiol* 2020; 19: 1725–1740.

[10] Marcelli E, Bortolani B, Corazza I, et al. A Novel Sensorized Heart Valve Prosthesis: Preliminary In Vitro Evaluation. *Sensors 2018, Vol 18,*; 18. Epub ahead of print 13 November 2018. DOI: 10.3390/s18113905.

[11] Garrett A, Kim B, Sie EJ, et al. Simultaneous photoplethysmography and blood flow measurements towards the estimation of blood pressure using speckle contrast optical spectroscopy. *Biomed Opt Express* 2023; 14: 1594.

[12] Vennemann B, Obrist D, Rösgen T. A smartphone-enabled wireless and batteryless implantable blood flow sensor for remote monitoring of prosthetic heart valve function. *PLoS One* 2020; 15: e0227372.

[13] Bailoor S, Seo JH, Dasi L, et al. Towards Longitudinal Monitoring of Leaflet Mobility in Prosthetic Aortic Valves via In-Situ Pressure Sensors: In-Silico Modeling and Analysis. *Cardiovasc Eng Technol* 2023; 14: 25–36.

[14] Gironi C, Cercenelli L, Bortolani B, et al. Innovative IntraValvular Impedance Sensing Applied to Biological Heart Valve Prostheses: Design and In Vitro Evaluation. *Sensors 2022, Vol 22,*; 22. Epub ahead of print 29 October 2022. DOI: 10.3390/s22218297.

[15] Basic Anatomy of the Human Heart - Cardiology Associates of Michigan - Michigan's Best Heart Doctors, https://www.cardofmich.com/anatomy-human-heart-fun-facts/ (accessed 13 March 2026).

[16] Murillo H, Lane MJ, Punn R, et al. Imaging of the aorta: embryology and anatomy. *Semin Ultrasound CT MR* 2012; 33: 169–190.

[17] Nagpal P, Agrawal MD, Saboo SS, et al. Imaging of the aortic root on high-pitch non-gated and ECG-gated CT: awareness is the key! *Insights Imaging*; 11. Epub ahead of print 1 December 2020. DOI: 10.1186/s13244-020-00855-w.
[18] Bissell MM, Dall'Armellina E, Choudhury RP. Flow vortices in the aortic root: in vivo 4D-MRI confirms predictions of Leonardo da Vinci. *Eur Heart J* 2014; 35: 1344.
[19] Braunwald's heart disease : a textbook of cardiovascular medicine - National Institutes of Health, https://onesearch.nihlibrary.ors.nih.gov/discovery/fulldisplay/alma991001193429704686/01NIH_INST:NIH (accessed 19 March 2026).
[20] Vesely I. The role of elastin in aortic valve mechanics. *J Biomech* 1997; 31: 115–123.
[21] Chen JH, Simmons CA. Cell-matrix interactions in the pathobiology of calcific aortic valve disease: critical roles for matricellular, matricrine, and matrix mechanics cues. *Circ Res* 2011; 108: 1510–1524.
[22] Nishimura RA. Cardiology patient pages. Aortic valve disease. *Circulation* 2002; 106: 770–772.
[23] Dweck MR, Boon NA, Newby DE. Calcific aortic stenosis: A disease of the valve and the myocardium. *J Am Coll Cardiol* 2012; 60: 1854–1863.
[24] Carabello BA, Paulus WJ. Aortic stenosis. *The Lancet* 2009; 373: 956–966.
[25] Stages of aortic stenosis - Guys and St Thomas Specialist Care, https://guysandstthomasspecialistcare.co.uk/news/stages-of-aortic-stenosis/ (accessed 13 March 2026).
[26] Siu SC, Silversides CK. Bicuspid Aortic Valve Disease. *J Am Coll Cardiol* 2010; 55: 2789–2800.
[27] Bates ER. Treatment Options in Severe Aortic Stenosis. Epub ahead of print 2011. DOI: 10.1161/CIRCULATIONAHA.110.974204.
[28] Nishimura RA, Otto CM, Bonow RO, et al. 2014 AHA/ACC guideline for the management of patients with valvular heart disease: A report of the American College of Cardiology/American Heart Association Task Force on Practice Guidelines. *J Thorac Cardiovasc Surg* 2014; 148: e1–e132.
[29] Nishimura RA, Otto CM, Bonow RO, et al. 2017 AHA/ACC Focused Update of the 2014 AHA/ACC Guideline for the Management of Patients With Valvular Heart Disease: A Report of the American College of Cardiology/American Heart Association Task Force on Clinical Practice Guidelines. *J Am Coll Cardiol* 2017; 70: 252–289.
[30] Leon MB, Smith CR, Mack MJ, et al. Transcatheter or Surgical Aortic-Valve Replacement in Intermediate-Risk Patients. *New England Journal of Medicine* 2016; 374: 1609–1620.
[31] Rayner C, Adams H. Aortic stenosis and transcatheter aortic valve implantation in the elderly. *Aust J Gen Pract* 2023; 52: 458–463.
[32] Wiegerinck EMA, Van Kesteren F, Van Mourik MS, et al. An up-to-date overview of the most recent transcatheter implantable aortic valve prostheses. *Expert Rev Med Devices* 2016; 13: 31–45.
[33] Binder RK, Rodés-Cabau J, Wood DA, et al. Transcatheter aortic valve replacement with the SAPIEN 3: A new balloon-expandable transcatheter heart valve. *JACC Cardiovasc Interv* 2013; 6: 293–300.
[34] Auricchio F, Taylor RL, Lubliner J. Shape-memory alloys: macromodelling and numerical simulations of the superelastic behavior. *Comput Methods Appl Mech Eng* 1997; 146: 281–312.
[35] Vinayak M, Leone PP, Tanner R, et al. Transcatheter Aortic Valve Replacement: Current Status and Future Indications. *J Clin Med*; 13. Epub ahead of print 1 January 2024. DOI: 10.3390/jcm13020373.

[36] Popma JJ, Deeb GM, Yakubov SJ, et al. Transcatheter Aortic-Valve Replacement with a Self-Expanding Valve in Low-Risk Patients. *N Engl J Med* 2019; 380: 1706–1715.
[37] Van Belle E, Vincent F, Labreuche J, et al. Balloon-Expandable Versus Self-Expanding Transcatheter Aortic Valve Replacement A Propensity-Matched Comparison From the FRANCE-TAVI Registry. *Circulation* 2020; 141: 243–259.
[38] Claessen BE, Tang GHL, Kini AS, et al. Considerations for Optimal Device Selection in Transcatheter Aortic Valve Replacement: A Review. *JAMA Cardiol* 2021; 6: 102–112.
[39] Leon MB, Smith CR, Mack M, et al. Transcatheter Aortic-Valve Implantation for Aortic Stenosis in Patients Who Cannot Undergo Surgery. *New England Journal of Medicine* 2010; 363: 1597–1607.
[40] Reardon MJ, Van Mieghem NM, Popma JJ, et al. Surgical or Transcatheter Aortic-Valve Replacement in Intermediate-Risk Patients. *New England Journal of Medicine* 2017; 376: 1321–1331.
[41] Mack MJ, Leon MB, Thourani VH, et al. Transcatheter Aortic-Valve Replacement with a Balloon-Expandable Valve in Low-Risk Patients. *New England Journal of Medicine* 2019; 380: 1695–1705.
[42] Thyregod HGH, Steinbrüchel DA, Ihlemann N, et al. No clinical effect of prosthesis–patient mismatch after transcatheter versus surgical aortic valve replacement in intermediate- and low-risk patients with severe aortic valve stenosis at mid-term follow-up: an analysis from the NOTION trial. *European Journal of Cardio-Thoracic Surgery* 2016; 50: 721–728.
[43] Mao W, Wang Q, Kodali S, et al. Numerical Parametric Study of Paravalvular Leak Following a Transcatheter Aortic Valve Deployment Into a Patient-Specific Aortic Root. *J Biomech Eng*; 140. Epub ahead of print 1 October 2018. DOI: 10.1115/1.4040457.
[44] Rotman OM, Bianchi M, Ghosh RP, et al. Principles of TAVR Valve Design, Modelling, and Testing. *Expert Rev Med Devices* 2018; 15: 771.
[45] Dvir D, Bourguignon T, Otto CM, et al. Standardized Definition of Structural Valve Degeneration for Surgical and Transcatheter Bioprosthetic Aortic Valves. *Circulation* 2018; 137: 388–399.
[46] Grunkemeier GL, Jamieson WRE, Miller DC, et al. Actuarial versus actual risk of porcine structural valve deterioration. *J Thorac Cardiovasc Surg* 1994; 108: 709–718.
[47] Schoen FJ, Levy RJ. Calcification of tissue heart valve substitutes: Progress toward understanding and prevention. *Annals of Thoracic Surgery* 2005; 79: 1072–1080.
[48] Butany J, Leask R. The failure modes of biological prosthetic heart valves. *J Long Term Eff Med Implants* 2001; 11: 115–135.
[49] Head SJ, Çelik M, Kappetein AP. Mechanical versus bioprosthetic aortic valve replacement. *Eur Heart J* 2017; 38: 2183–2191.
[50] Hsu MC, Kamensky D, Bazilevs Y, et al. Fluid–structure interaction analysis of bioprosthetic heart valves: Significance of arterial wall deformation. *Comput Mech* 2014; 54: 1055.
[51] Vennemann B, Rösgen T, Heinisch PP, et al. Leaflet Kinematics of Mechanical and Bioprosthetic Aortic Valve Prostheses. *ASAIO J* 2018; 64: 651–661.
[52] Costa G, Criscione E, Todaro D, et al. Long-term Transcatheter Aortic Valve Durability. *Interv Cardiol* 2019; 14: 62–69.
[53] Makkar RR, Fontana G, Jilaihawi H, et al. Possible Subclinical Leaflet Thrombosis in Bioprosthetic Aortic Valves. *N Engl J Med* 2015; 373: 2015–2024.
[54] Kappetein AP, Head SJ, Généreux P, et al. Updated standardized endpoint definitions for transcatheter aortic valve implantation: the Valve Academic Research

Consortium-2 consensus document. *Eur Heart J*; 33. Epub ahead of print October 2012. DOI: 10.1093/eurheartj/ehs255.

[55] Ross J, Braunwald E. Aortic stenosis. *Circulation* 1968; 38: 61–67.

[56] Khan JM, Greenbaum AB, Babaliaros VC, et al. BASILICA Trial: One-Year Outcomes of Transcatheter Electrosurgical Leaflet Laceration to Prevent TAVR Coronary Obstruction. *Circ Cardiovasc Interv* 2021; 14: E010238.

[57] Pache G, Schoechlin S, Blanke P, et al. Early hypo-attenuated leaflet thickening in balloon-expandable transcatheter aortic heart valves. *Eur Heart J* 2016; 37: 2263–2271.

[58] Hansson NC, Grove EL, Andersen HR, et al. Transcatheter Aortic Valve Thrombosis: Incidence, Predisposing Factors, and Clinical Implications. *J Am Coll Cardiol* 2016; 68: 2059–2069.

[59] Leetmaa T, Hansson NC, Leipsic J, et al. Early aortic transcatheter heart valve thrombosis: diagnostic value of contrast-enhanced multidetector computed tomography. *Circ Cardiovasc Interv*; 8. Epub ahead of print 21 April 2015. DOI: 10.1161/CIRCINTERVENTIONS.114.001596.

[60] Zoghbi WA, Chambers JB, Dumesnil JG, et al. Recommendations for Evaluation of Prosthetic Valves With Echocardiography and Doppler Ultrasound. A Report From the American Society of Echocardiography's Guidelines and Standards Committee and the Task Force on Prosthetic Valves, Developed in Conjunctio…. *Journal of the American Society of Echocardiography* 2009; 22: 975–1014.

[61] Otto CM, Nishimura RA, Bonow RO, et al. 2020 ACC/AHA Guideline for the Management of Patients With Valvular Heart Disease: A Report of the American College of Cardiology/American Heart Association Joint Committee on Clinical Practice Guidelines. *Circulation* 2021; 143: E72–E227.

[62] Stewart WJ. Thrombosis of Bioprosthetic Valves: Can We Afford to Ignore It? *J Am Coll Cardiol* 2015; 66: 2295–2297.

[63] Dangas GD, Weitz JI, Giustino G, et al. Prosthetic Heart Valve Thrombosis. *J Am Coll Cardiol* 2016; 68: 2670–2689.

[64] Lindman BR, Clavel MA, Mathieu P, et al. Calcific aortic stenosis. *Nat Rev Dis Primers*; 2. Epub ahead of print 3 March 2016. DOI: 10.1038/nrdp.2016.6.

[65] Vlachopoulos C, Aznaouridis K, Stefanadis C. Prediction of Cardiovascular Events and All-Cause Mortality With Arterial Stiffness. A Systematic Review and Meta-Analysis. *J Am Coll Cardiol* 2010; 55: 1318–1327.

[66] Ben-Shlomo Y, Spears M, Boustred C, et al. Aortic pulse wave velocity improves cardiovascular event prediction: An individual participant meta-analysis of prospective observational data from 17,635 subjects. *J Am Coll Cardiol* 2014; 63: 636–646.

[67] Zheng D, Yao Y, Morrison I, et al. Photoplethysmographic assessment of arterial stiffness and endothelial function. *Photoplethysmography: Technology, Signal Analysis and Applications* 2021; 235–276.

[68] Laurent S, Cockcroft J, Van Bortel L, et al. Expert consensus document on arterial stiffness: methodological issues and clinical applications. *Eur Heart J* 2006; 27: 2588–2605.

[69] Broyd CJ, Patel K, Pugliese F, et al. Pulse wave velocity can be accurately measured during transcatheter aortic valve implantation and used for post-procedure risk stratification. *J Hypertens* 2019; 37: 1845–1852.

[70] Terentes-Printzios D, Gardikioti V, Aznaouridis K, et al. The impact of transcatheter aortic valve implantation on arterial stiffness and wave reflections. *Int J Cardiol* 2021; 323: 213–219.

[71] Osawa A, Ikenaga H, Kuraishi A, et al. Exercise-induced brachial-ankle pulse wave velocity changes before and after transcatheter aortic valve replacement. *Heart*

Vessels; 41. Epub ahead of print 1 February 2026. DOI: 10.1007/s00380-025-02593-9.

[72] Williams B, Mancia G, Spiering W, et al. 2018 ESC/ESH Guidelines for the management of arterial hypertension. *Eur Heart J* 2018; 39: 3021–3104.

[73] Levy BI, Tedgui A (eds). Biology of the Arterial Wall. 1. Epub ahead of print 1999. DOI: 10.1007/b102335.

[74] Bramwell JC, Hill AV. The velocity of pulse wave in man. *Proceedings of the Royal Society of London Series B, Containing Papers of a Biological Character* 1922; 93: 298–306.

[75] Townsend RR, Wilkinson IB, Schiffrin EL, et al. Recommendations for Improving and Standardizing Vascular Research on Arterial Stiffness: A Scientific Statement from the American Heart Association. *Hypertension* 2015; 66: 698–722.

[76] Greenwald SE. Ageing of the conduit arteries. *Journal of Pathology* 2007; 211: 157–172.

[77] Allen J. Photoplethysmography and its application in clinical physiological measurement. *Physiol Meas* 2007; 28: R1.

[78] Alian AA, Shelley KH. PPG in clinical monitoring. *Photoplethysmography: Technology, Signal Analysis and Applications* 2021; 341–359.

[79] Millasseau SC, Kelly RP, Ritter JM, et al. Determination of age-related increases in large artery stiffness by digital pulse contour analysis. *Clin Sci (Lond)* 2002; 103: 371–377.

[80] Asada HH, Shaltis P, Reisner A, et al. Mobile monitoring with wearable photoplethysmographic biosensors. *IEEE Eng Med Biol Mag* 2003; 22: 28–40.

[81] Maeda Y, Sekine M, Tamura T. The advantages of wearable green reflected photoplethysmography. *J Med Syst* 2011; 35: 829–834.

[82] Tamura T. Current progress of photoplethysmography and SPO2 for health monitoring. *Biomed Eng Lett* 2019; 9: 21–36.

[83] Nomoni M, May JM, Kyriacou PA. Novel Polydimethylsiloxane (PDMS) Pulsatile Vascular Tissue Phantoms for the In-Vitro Investigation of Light Tissue Interaction in Photoplethysmography. *Sensors 2020, Vol 20,* 2020; 20: 1–13.

[84] Nwafor CI, Plant KD, King DR, et al. Assessment of a noninvasive optical photoplethysmography imaging device with dynamic tissue phantom models. *J Biomed Opt* 2017; 22: 1.

[85] Paul M, Mota AF, Antink CH, et al. Modeling photoplethysmographic signals in camera-based perfusion measurements: optoelectronic skin phantom. *Biomed Opt Express* 2019; 10: 4353.

[86] Rivero G, García-Páez JM, Alvarez L, et al. Magnetic sensor for early detection of heart valve bioprostheses failure. *Sens Lett* 2007; 5: 263–266.

[87] Lanning C, Shandas R. Development and validation of implantable sensors for monitoring function of prosthetic heart valves: in vitro studies. *Med Biol Eng Comput* 2003; 41: 416–424.

[88] Bailoor S, Seo JH, Dasi L, et al. Prosthetic Valve Monitoring via In Situ Pressure Sensors: In Silico Concept Evaluation using Supervised Learning. *Cardiovascular Engineering and Technology 2021 13:1* 2021; 13: 90–103.

[89] Vennemann B, Obrist D, Rösgen T. Automated diagnosis of heart valve degradation using novelty detection algorithms and machine learning. *PLoS One*; 14. Epub ahead of print 1 September 2019. DOI: 10.1371/journal.pone.0222983.

[90] Liu R, Li Q, Li Y, et al. A new wearable e monitoring technology for evaluation of left ventricular remodeling after transcatheter aortic valve replacement. *European Heart Journal - Digital Health* 2025; 6: 713–722.

[91] Kwon K, Kim JU, Won SM, et al. A battery-less wireless implant for the continuous monitoring of vascular pressure, flow rate and temperature. *Nature Biomedical Engineering 2023 7:10* 2023; 7: 1215–1228.
[92] Naccarata F, Occhiuzzi C, Verzicco R, et al. Wireless and Zero-Power Trans-Cardiac Link With Antennified Aortic Valve Bioprostheses. *IEEE J Electromagn RF Microw Med Biol* 2023; 7: 15–23.
[93] Dasi LP, Hatoum H, Kheradvar A, et al. On The Mechanics of Transcatheter Aortic Valve Replacement. *Ann Biomed Eng* 2016; 45: 310.
[94] Anam SB, Kovarovic BJ, Ghosh RP, et al. Assessment of Paravalvular Leak Severity and Thrombogenic Potential in Transcatheter Bicuspid Aortic Valve Replacements Using Patient-Specific Computational Modeling. *J Cardiovasc Transl Res* 2022; 15: 834–844.
[95] Morganti S, Conti M, Aiello M, et al. Simulation of transcatheter aortic valve implantation through patient-specific finite element analysis: two clinical cases. *J Biomech* 2014; 47: 2547–2555.
[96] Pasta S, Cannata S, Gentile G, et al. Simulation study of transcatheter heart valve implantation in patients with stenotic bicuspid aortic valve. *Med Biol Eng Comput* 2020; 58: 815–829.
[97] Bailey J, Curzen N, Bressloff NW. Assessing the impact of including leaflets in the simulation of TAVI deployment into a patient-specific aortic root. *Comput Methods Biomech Biomed Engin* 2016; 19: 733–744.
[98] Wang Q, Kodali S, Primiano C, et al. Simulations of transcatheter aortic valve implantation: implications for aortic root rupture. *Biomech Model Mechanobiol* 2015; 14: 29–38.
[99] Catalano C, Crascì F, Puleo S, et al. Computational fluid dynamics in cardiac surgery and perfusion: A review. *Perfusion* 2025; 40: 362–370.
[100] Sturla F, Ronzoni M, Vitali M, et al. Impact of different aortic valve calcification patterns on the outcome of transcatheter aortic valve implantation: A finite element study. *J Biomech* 2016; 49: 2520.
[101] Basri AA, Zuber M, Basri EI, et al. Fluid Structure Interaction on Paravalvular Leakage of Transcatheter Aortic Valve Implantation Related to Aortic Stenosis: A Patient-Specific Case. *Comput Math Methods Med* 2020; 2020: 9163085.
[102] Nappi F, Mazzocchi L, Timofeva I, et al. A Finite Element Analysis Study from 3D CT to Predict Transcatheter Heart Valve Thrombosis. *Diagnostics* 2020; 10: 183.
[103] McGee OM, Gunning PS, McNamara A, et al. The impact of implantation depth of the Lotus^{TM} valve on mechanical stress in close proximity to the bundle of His. *Biomech Model Mechanobiol* 2019; 18: 79–88.
[104] Finotello A, Morganti S, Auricchio F. Finite element analysis of TAVI: Impact of native aortic root computational modeling strategies on simulation outcomes. *Med Eng Phys* 2017; 47: 2.
[105] Russ C, Hopf R, Hirsch S, et al. Simulation of transcatheter aortic valve implantation under consideration of leaflet calcification. *Annu Int Conf IEEE Eng Med Biol Soc* 2013; 2013: 711–714.
[106] Morris PD, Narracott A, Von Tengg-Kobligk H, et al. Computational fluid dynamics modelling in cardiovascular medicine. *Heart* 2016; 102: 18–28.
[107] Bianchi M, Ghosh RP, Marom G, et al. Simulation of Transcatheter Aortic Valve Replacement in patient-specific aortic roots: Effect of crimping and positioning on device performance. *Proceedings of the Annual International Conference of the IEEE Engineering in Medicine and Biology Society, EMBS* 2015; 2015-November: 282–285.

[108] Catalano C, Cannata S, Gandolfo C, et al. An Inverse Analysis for the Assessment of Material Properties of TAVI Patients, https://iris.unipa.it/handle/10447/618019 (2023, accessed 18 March 2026).
[109] Bosi GM, Capelli C, Cheang MH, et al. Population-specific material properties of the implantation site for transcatheter aortic valve replacement finite element simulations. *J Biomech* 2018; 71: 236.
[110] Mao W, Li K, Sun W. Fluid-Structure Interaction Study of Transcatheter Aortic Valve Dynamics Using Smoothed Particle Hydrodynamics. *Cardiovasc Eng Technol* 2016; 7: 374–388.
[111] Biffi B, Gritti M, Grasso A, et al. A workflow for patient-specific fluid–structure interaction analysis of the mitral valve: A proof of concept on a mitral regurgitation case. *Med Eng Phys* 2019; 74: 153–161.
[112] Chandran KB, Vigmostad SC. Patient-specific bicuspid valve dynamics: Overview of methods and challenges. *J Biomech* 2013; 46: 208–216.
[113] Hsu MC, Kamensky D, Xu F, et al. Dynamic and fluid–structure interaction simulations of bioprosthetic heart valves using parametric design with T-splines and Fung-type material models. *Comput Mech* 2015; 55: 1211.
[114] Luraghi G, Migliavacca F, García-González A, et al. On the Modeling of Patient-Specific Transcatheter Aortic Valve Replacement: A Fluid-Structure Interaction Approach. *Cardiovasc Eng Technol* 2019; 10: 437–455.
[115] Sun W, Mao W, Griffith BE. Computer modeling and simulation of heart valve function and intervention. *Principles of Heart Valve Engineering* 2019; 177–211.
[116] Lluch È, De Craene M, Bijnens B, et al. Breaking the state of the heart: meshless model for cardiac mechanics. *Biomech Model Mechanobiol* 2019; 18: 1549–1561.
[117] Morany A, Lavon K, Gomez Bardon R, et al. Fluid–structure interaction modeling of compliant aortic valves using the lattice Boltzmann CFD and FEM methods. *Biomech Model Mechanobiol* 2023; 22: 837–850.
[118] Puleo S, Pasta S, Scardulla F, et al. Fluid–Solid Interaction Analysis for Developing In-Situ Strain and Flow Sensors for Prosthetic Valve Monitoring. *Sensors 2024, Vol 24,*; 24. Epub ahead of print 4 August 2024. DOI: 10.3390/s24155040.
[119] Verstraeten SCFPM. Modelling Aortic Stenosis: Towards clinical decision support and in silico trials, https://research.tue.nl/en/publications/modelling-aortic-stenosis-towards-clinical-decision-support-and-i/ (2026, accessed 19 March 2026).
[120] Xu KW, Gao Q, Wan M, et al. Mock circulatory loop applications for testing cardiovascular assist devices and in vitro studies. *Front Physiol* 2023; 14: 1175919.
[121] Cappon F, Wu T, Papaioannou T, et al. Mock circulatory loops used for testing cardiac assist devices: A review of computational and experimental models. *Int J Artif Organs* 2021; 44: 793–806.
[122] Westerhof N, Elzinga G, Sipkema P. An artificial arterial system for pumping hearts. *J Appl Physiol* 1971; 31: 776–781.
[123] Cercenelli L, Gironi C, Bortolani B, et al. First Ex Vivo Animal Study of a Biological Heart Valve Prosthesis Sensorized with Intravalvular Impedance. *Sensors 2023, Vol 23,*; 23. Epub ahead of print 8 April 2023. DOI: 10.3390/s23083829.
[124] Cutugno S, Agnese V, Gentile G, et al. Patient-Specific Analysis of Ascending Thoracic Aortic Aneurysm with the Living Heart Human Model. *Bioengineering 2021, Vol 8,*; 8. Epub ahead of print 4 November 2021. DOI: 10.3390/BIOENGINEERING8110175.
[125] D'Humières D, Ginzburg I, Krafczyk M, et al. Multiple-relaxation-time lattice Boltzmann models in three dimensions. *Philos Trans A Math Phys Eng Sci* 2002; 360: 437–451.
[126] Chen L, Yu Y, Hou G. Sharp-interface immersed boundary lattice Boltzmann method with reduced spurious-pressure oscillations for moving boundaries. *Phys Rev E Stat*

Nonlin Soft Matter Phys; 87. Epub ahead of print 31 May 2013. DOI: 10.1103/PhysRevE.87.053306.

[127] D'Humières D, Ginzburg I, Krafczyk M, et al. Multiple-relaxation-time lattice Boltzmann models in three dimensions. *Philosophical Transactions of the Royal Society A: Mathematical, Physical and Engineering Sciences* 2002; 360: 437–451.

[128] Chen L, Yu Y, Hou G. Sharp-interface immersed boundary lattice Boltzmann method with reduced spurious-pressure oscillations for moving boundaries. *Phys Rev E* 2013; 87: 053306.

[129] Pasta S, Cannata S, Gentile G, et al. Transcatheter Heart Valve Implantation in Bicuspid Patients with Self-Expanding Device. *Bioengineering (Basel)*; 8. Epub ahead of print 1 July 2021. DOI: 10.3390/bioengineering8070091.

[130] Abbasi M, Qiu D, Behnam Y, et al. High resolution three-dimensional strain mapping of bioprosthetic heart valves using digital image correlation. *J Biomech* 2018; 76: 27–34.

[131] Lo Presti D, Massaroni C, Jorge Leitao CS, et al. Fiber bragg gratings for medical applications and future challenges: A review. *IEEE Access* 2020; 8: 156863–156888.

[132] D'Acquisto L, Scardulla F, Pasta S. Steam sterilization processes affect the stability of clinical thermometers: Thermistor and prototypal FBG probe comparison. *Optical Fiber Technology* 2020; 55: 102156.

[133] Wilson JS, Taylor WR, Oshinski J. Assessment of the regional distribution of normalized circumferential strain in the thoracic and abdominal aorta using DENSE cardiovascular magnetic resonance. *Journal of Cardiovascular Magnetic Resonance*; 21. Epub ahead of print 16 September 2019. DOI: 10.1186/s12968-019-0565-0.

[134] Satriano A, Guenther Z, White JA, et al. Three-dimensional thoracic aorta principal strain analysis from routine ECG-gated computerized tomography: feasibility in patients undergoing transcatheter aortic valve replacement. *BMC Cardiovasc Disord*; 18. Epub ahead of print 2 May 2018. DOI: 10.1186/s12872-018-0818-0.

[135] Puleo S, Diana G, Pasta S, et al. Sensor-Based Bioprosthetic Valve Monitoring: Numerical Simulation and Experimental Design. *Lecture Notes in Mechanical Engineering* 2025; 44–51.

[136] Belz GG. Elastic properties and Windkessel function of the human aorta. *Cardiovasc Drugs Ther* 1995; 9: 73–83.

[137] Laurent S, Boutouyrie P, Asmar R, et al. Aortic stiffness is an independent predictor of all-cause and cardiovascular mortality in hypertensive patients. *Hypertension* 2001; 37: 1236–1241.

[138] Diana G, Scardulla F, Puleo S, et al. Non-Invasive Estimation of Arterial Stiffness Using Photoplethysmography Sensors: An In Vitro Approach. *Sensors 2025, Vol 25,*; 25. Epub ahead of print 24 May 2025. DOI: 10.3390/s25113301.

[139] Puleo S, Diana G, Livolsi C, et al. Non-Invasive Monitoring of Transcatheter Heart Valve Using Photoplethysmography and Machine Learning. *Artif Organs* 2025; 0: 1–7.

[140] Pasta S, Scardulla F, Rinaudo A, et al. An In Vitro Phantom Study on the Role of the Bird-Beak Configuration in Endograft Infolding in the Aortic Arch. *J Endovasc Ther* 2016; 23: 172–181.

[141] Scardulla F, Bellavia D, D'Acquisto L, et al. Particle image velocimetry study of the celiac trunk hemodynamic induced by continuous-flow left ventricular assist device. *Med Eng Phys* 2017; 47: 47.

[142] Wilson RD, Vardanega S, Chen J, et al. The Impact of Aortic Valve Stenosis on Pulse Wave Morphology: An in silico study with 16,038 virtual subjects, https://kclpure.kcl.ac.uk/portal/en/publications/the-impact-of-aortic-valve-stenosis-on-pulse-wave-morphology-an-i/ (2025, accessed 17 April 2026).

[143] Plunde O, Franco-Cereceda A, Bäck M. Pulse Wave Morphology Changes in Aortic Valve Stenosis Detected with Cardio-Ankle Vascular Index. *Vasc Health Risk Manag* 2023; 19: 325.
[144] Mukkamala R, Shroff SG, Landry C, et al. The Microsoft Research Aurora Project: Important Findings on Cuffless Blood Pressure Measurement. *Hypertension* 2022; 80: 534.